Semi-analytic solutions to edge singularities of three-dimensional axisymmetric bodies

Yixin, Qian
State Key Laboratory of Coastal and Offshore Engineering, Dalian University of Technology

Bin, Teng
State Key Laboratory of Coastal and Offshore Engineering, Dalian University of Technology

Liu, Yingyi
Research Institute for Applied Mechanics, Kyushu University

出版情報：Physics of Fluids. 35 (6), pp.067127-, 2023-06-23. American Institute of Physics : AIP
バージョン：
権利関係：

Semi-Analytic Solutions to Edge Singularities of Three-dimensional Axisymmetric Bodies

Yixin Qian (钱弈心)[1], Bin Teng (滕斌)[1,*], Yingyi Liu (刘盈溢)[2]

[1] State Key Laboratory of Coastal and Offshore Engineering, Dalian University of Technology, Dalian 116024, China

[2] Research Institute for Applied Mechanics, Kyushu University, Fukuoka 8168580, Japan

* Corresponding author, e-mail address: bteng@dlut.edu.cn

Abstract

Axisymmetric geometries, such as cylindrical elements, are widely used in offshore structures. However, the presence of sharp edges in these geometries introduces challenges in numerical simulations due to singularities. To address this issue, one possible solution is to represent the singularities using analytic eigenfunctions. This approach can provide insights into the essence of the problem and has successfully applied to two-dimensional (2D) corner problems. However, finding appropriate eigenfunctions for the three-dimensional (3D) edges remains an open challenge. This paper proposes a semi-analytic scheme for 3D axisymmetric problems utilizing a scaled boundary finite element method (SBFEM). A dimensional reduction is introduced to the 3D Laplace equation, and a 3D edge is handled on the generatrix plane while governed by a complicated equation. The algorithm for resolving the SBFEM fundamental space is improved, and the singularities are approximated using a fractional-order basis. The effectiveness of the proposed method is demonstrated through its application to solve the radiation problem of a heaving cylinder. The method accurately captures the singular velocity field at the edge tip, ensuring that the boundary condition on the body surface is strictly satisfied in the neighborhood of the singularity. Accuracy of the mean drift force is ensured by performing direct pressure integrations over the body surface using a near-

field formulation, which becomes as accurate as the middle-field formulation.

Keywords: scaled boundary finite element method; axisymmetric singularity; potential flow

1 Introduction

With the advancement of offshore technology, the exploitation of marine resources has been stretched out to the open sea. Under increasing water depths and hostile environmental conditions, floating infrastructures are required with higher performance and reliability. Hydrodynamic analysis plays a crucial role in the design and construction. Axisymmetric bodies not only play an important role in academic scenarios but also has wide applications in practical engineering. For example, cylinders are representative as central components in spars platforms and as pontoons of semi-submersible platforms; circular discs are widely used as heave plates in spars and power take-off devices of wave energy convectors (WECs). Specialized methods have been proposed by, for example, Hulme (1983), Kim and Yue (1989, 1990) and Teng and Kato (1999, 2002), to tackle axisymmetric problems. The hydrodynamic characteristics of these structures possess both academic and practical value, leading to an increasing number of studies in recent years with an engineering purpose. For example, Wang and Yeung (2019) developed a hybrid integral-equation method for point-absorber WECs; Chanda et al. (2022) and Sarkar and Chanda (2022) investigated the structural performance of porous cylinders on a porous seabed; Das et al. (2022, 2023) studied the behavior of discs submerged in two- and three-layer fluids; Porter (2015) proposed an efficient method for wave radiation and diffraction by circular plates, and this work has been extended to permeable plates in an array by Zheng et al. (2023) and Liang et al. (2021) and to nearly circular plates by Farina et al. (2017).

The potential flow model is widely used to simulate the hydrodynamics of large-scale offshore structures. It assumes ideal fluids with no vorticity, and the fluid velocity is represented as the spatial gradient of a velocity potential. While this model facilitates numerical calculations, the accuracy of the fluid velocity, especially at the boundaries, is lower compared to the potential.

Refinements in discretization, including diminishing the element size (viz., *h*-method) and improving the interpolation order (viz., *p*-method), are generally effective for higher accuracy. However, these refinements encounter challenges when dealing with structures with sharp profiles. The presence of sharp edges on the body surface gives rise to singularities, where the velocity becomes infinite.

From a mathematical perspective, singularities are commonly encountered in elliptic equations at sharp corners and edges where the boundary conditions are discontinuous. This difficulty has nearly become a common concern and is pronounced for the extensively studied cylindrical bodies. For example, Lee (2007) demonstrated that the pressure integration for the mean drift force becomes divergent in the case of a truncated cylinder, compared with the satisfying case of a sphere. Yang et al. (2020) investigated the impact of sharp edges on cylindrical bodies, revealing that the edge effect leads to erroneous gradients, wave forces, and time derivatives.

If the field quantities are not of concern, indirect methods provide alternatives for boundary integrations. These methods are developed based on two main concepts. The first concept is using integration transformations. Researchers such as Molin (1979), Lighthill (1979), and Eatock Taylor and Hung (1987) devised indirect schemes to integrate the second-order potential on the body surface without directly solving the challenging second-order potential itself. Cong et al. (2020) further reduced the quadratic product of gradients in the body surface integrations using Gauss' theorem. Dai et al. (2005) and Chen (2007) proposed a middle-field formulation for second-order low-frequency and mean drift forces using Gauss' and Stokes' theorems. The second concept is following momentum conservation. Zhao and Faltinesen (1989) and Lee (2007) obtained accurate mean drift force by applying this principle. Sclavounos (2012) and Gadi et al. (2018) extended the application to include full wave force components. These indirect methods are proposed for particular purposes but do not fundamentally address the singularity issue.

Improving the numerical solvers is recommended as a straightforward and comprehensive approach to handling singularities. Over the years, various solvers have been developed and proposed to address this challenge. These solvers include boundary element methods (BEMs), e.g., Yang and

Ertekin (1992), Teng and Eatock Taylor (1995), Kashiwagi et al. (1998), Newman and Lee (2002); finite element methods (FEMs), e.g., Wu and Eatock Taylor (1994), Ma et al. (2001a, b); finite difference methods (FDMs), e.g., Bingham and Zhang (2007), Engsig Karup et al. (2009); harmonic polynomial cell (HPC) methods, e.g., Shao and Faltinsen (2012, 2014a, b), Hanssen and Greco (2021). For a smooth variation (i.e., when the weak derivatives are continuous), the solution space can be embedded by appropriate regular basis spaces as $H^{k\in\mathbb{N}_+}$, for example, the polynomial basis. Therefore, from a mathematical perspective, these solvers are impeccable. For a singular variation, however, the solution lies in a fractional-order space, and the regular basis becomes inadequate. To address this issue, several numerical methods have been developed by supplementing the regular test/basis space with singular representations. One such method is the multi-term Galerkin method (MGM), which improves upon the traditional matched eigenfunction expansion method (MEEM) by taking a fractional-order function as the test function to match the interfaces. The drawback is that it is applied to simple geometries, e.g., barriers (Porter and Evans, 1995; Martins Rivas and Mei, 2009), cylinders (Li and Liu, 2019; Li et al., 2019), and sectors (Chang et al., 2012). A boundary integral method, utilizing orthogonal functions for boundary interpolations, can achieve similar effects. Porter (2015) researched the linear diffraction/radiation problems of submerged discs, employing Gegenbauer polynomials to represent the square root of the solutions. This concept can also be referred to in Martin and Llewellyn Smith (2011) and Zheng et al. (2023). Notably, rapid numerical convergence was observed, leading to accurate computations of the body surface quantities. The extended finite element method (XFEM), also known as the generalized finite element method (GFEM), was introduced by Belytschko and Black (1999) as a means to model discontinuities. The shape functions of tip-neighboring elements are enhanced, leading to notable success in fracture mechanics and other related scopes. Following the same idea, Liang et al. (2015) incorporated the eigenfunctions of two-dimensional (2D) corner flow into the HPC model and conducted extensive studies on bodies such as boxes, flat plates, and hydrofoils. Based on their practice, Wang et al. (2021) employed an XFEM in hydrodynamics and achieved a similar effect. Additionally, a dual-function-based FEM has been developed to decouple the singular part

from the variational equation. Cai and Kim (2001) and Cai et al. (2002, 2006) have applied this method to Possion problems, while Choi and Kweon (2013, 2016) have utilized it for stationary Navier-Stokes problems.

These enhanced methods are specifically designed to handle singularities. However, they typically rely on prior knowledge of the eigenfunctions of singularities. While within the potential flow theory framework, eigenfunctions for corners in the 2D Laplace equation have been known, they are not accessible for three-dimensional (3D) edges. As an alternative approach, we aim to analyze such problems using a semi-analytic approach. In this project, we employ the scaled boundary finite element method (SBFEM) as the basis for our analysis. The SBFEM was initially developed by Wolf and Song (1996) for the dynamic soil-structure interaction and has since evolved into a versatile solver in multiple scopes, such as elasticity and fracture mechanics (e.g., Long et al., 2014; Yang and Ooi, 2012; Hell and Becker, 2019), potential flow (Tao et al., 2007; Deeks and Cheng, 2003) and heat transfer (e.g., Bazyar and Talebi, 2015; Yu et al., 2021). In SBFEMs, solutions exhibit analytic behavior in the radial direction. The radial solution is inherent and can be fractional order satisfying the boundary condition, which forms the basis for modeling singularities. There are two algorithms for solving the fundamental spaces of the SBFEM system. The first is the eigenvalue (as presented by Song and Wolf, 1997, 2000) or Schur decomposition (as presented by Song, 2004), which is the common algorithm for elasticity, elastodynamics, and Laplace problems. The second is an asymptotic expansion technique, which is employed in the elastodynamic equation in the frequency domain, as proposed by Song and Wolf (1998) and Yang et al. (2007). However, as the mathematical formulations differ, the existing algorithms are incapable of our design. And thus, we have made some improvements to address this issue.

The primary focus of this study is to investigate the edge behaviors of axisymmetric bodies, serving as the initial step in the 3D analysis. This paper is structured as follows. Section 2 specifies generic basics on the edge singularities, including the dimensional reduction, the SBFEM concepts, and the derivation of the basis functions. Section 3 demonstrates the numerical formulations for problems involving edges by solving a linearized radiation problem. Two strategies are proposed

131 to implement the singularity simulation. Section 4 presents a case study involving a heaving trun-
132 cated cylinder. The potential and the velocity distributions on the body surface, the velocity field
133 in the edge neighborhood, and pressure integration are presented. Finally, some conclusions are
134 drawn.
135

2 Mathematical model of 3D axisymmetric singularities

The fluid is assumed as incompressible and inviscid, and the flow is irrotational. The velocity of the flow is described as the gradient field of the velocity potential, governed by the Laplace equation

$$\nabla \cdot \nabla \Phi = 0 \text{ , in } \Omega^3, \tag{2.1}$$

where Ω^3 is a computational fluid domain in the 3D space and $\Phi(\mathbf{x}, t)$ the velocity potential, dependent or independent of the time variable. But as the singularity discussed is a spatial behavior of the Laplacian, herein we omit the time variable t in expression and denote by $S(\mathrm{x})$ the local potential field containing a singular point.

2.1 Dimensional reduction for 3D axisymmetric problems

The disturbance by an axisymmetric body is focused. Without loss of generality, a body with an upward symmetric axis is exampled in Fig. 1. It is considered in an open area, and the body is not in contact with other bodies, such that we can always identify an axisymmetric region of the fluid, denoted by Ω^3, surrounding the body. The solutions are determined by the conditions on the enclosed boundary, represented as $\partial\Omega^3 = \partial\Omega^3_{\mathrm{b}} \cup \partial\Omega^3_{\mathrm{ex}}$, where $\partial\Omega^3_{\mathrm{b}}$ corresponds to the surface of the body and $\partial\Omega^3_{\mathrm{ex}}$ refers to other boundaries. By exploiting the geometric symmetry, the problem is expressed in terms of cylindrical coordinates where the r-z plane coincides with the generatrix and the circumference angle θ encircles the z-axis. A Fourier expansion is employed for the solution in the form of

$$\Phi = \Phi_0\left(r,z\right) + \sum\nolimits_{l=1}\left[\cos\left(l\theta\right)\Phi_l^{\cos}\left(r,z\right) + \sin\left(l\theta\right)\Phi_l^{\sin}\left(r,z\right)\right] \tag{2.2}$$

where Φ_0 $\Phi_l^{\cos}$, $\Phi_l^{\sin}$ are the dimensional-reduced potentials in the axial section, which are thus governed by the two-variable equations

$$\nabla \cdot \left(r\nabla \Phi_l\right) - \frac{l^2}{r}\Phi_l = 0 \text{ , in } \Omega^2, \tag{2.3}$$

where Φ_l refers to any of them. Ω^2, $\partial\Omega^2_{\mathrm{b}}$, and $\partial\Omega^2_{\mathrm{ex}}$ are, respectively, the dimensional-reductions

of Ω^3, $\partial\Omega_{\mathrm{b}}^3$, and $\partial\Omega_{\mathrm{ex}}^3$, as shown in Fig. 1. The superscripts 2 and 3 indicate the spatial dimension.

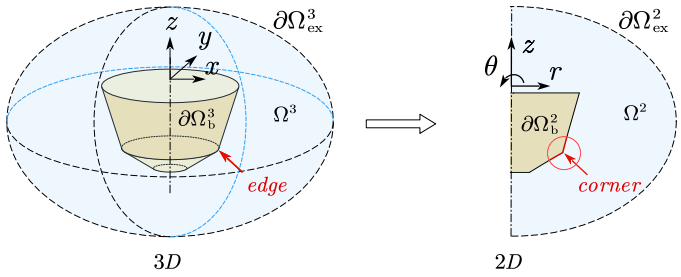

Fig. 1 Cylindrical coordinates for a 3D axisymmetric problem and the dimensional reduction to the generatrix plane

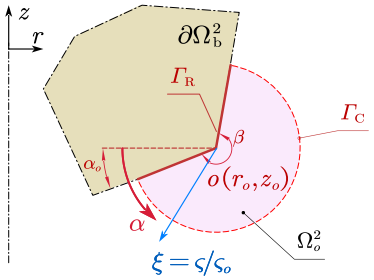

Fig. 2 Polar coordinates at a 2D corner on r-z plane

From a geometrical viewpoint, a 3D axisymmetric edge is the rotational path of a 2D corner in the generatrix section. With this understanding, tackling this issue becomes straightforward. If the corner behaviors in $\Phi_l(r,z)$ can be described, the edge representation in Φ is a weighted combination of the formers. However, the challenge lies in properly solving Eq. (2.3) while handling the singularities with care. To address it, we focus our attention on the singular local solution denoted by $S_l(r,z)$, defined in a neighborhood, Ω_o^2, of the corner tip (r_o, z_o) with a small radius ς_o, as illustrated in Fig. 2.

At the tip, a local polar coordinate system $o-\alpha\varsigma$ is established to describe Ω_o^2. ς and α represent the radial and circumferential variables, respectively, defining Ω_o^2 as $\{(\varsigma,\alpha) \in [0,\varsigma_o] \times [\alpha_o, \alpha_o+\beta]\}$. β is the angle of the corner on the generatrix plane, and α_o is the angle determining the orientation. Both angles are free variables that can vary from 0 to 2π. To simplify the notation, a radial variable ξ is introduced as a dimensionless radius, defined as $\xi = \varsigma/\varsigma_o$. The transformation between the two coordinate systems is given by

$$\begin{aligned} r &= r_o - \xi\zeta_o \cos\left(\alpha - \alpha_o\right) \\ z &= z_o - \xi\zeta_o \sin\left(\alpha - \alpha_o\right) \end{aligned}. \tag{2.4}$$

Two boundaries enclose Ω_o^2, i.e., $\partial\Omega_o^2 = \Gamma_{\mathrm{R}} \cup \Gamma_{\mathrm{C}}$. Γ_{R} denotes the radial boundary as $\Gamma_{\mathrm{R}} = \{(\xi,\alpha)|0 \le \xi \le 1, \alpha = \alpha_o \text{ or } \alpha_o + \beta\}$, which is a subsection of $\partial\Omega_{\mathrm{body}}^2$. The Γ_{R} condition is Neumann-type, as

$$\frac{1}{\zeta_o \xi}\frac{\partial \Phi_l}{\partial \alpha} = f_{\mathrm{b}}\left(\xi\right)\Big|_{\Gamma_{\mathrm{R}}}, \tag{2.5}$$

where f_{b} is the forcing term along the reentrant sides. Γ_{C} denotes the circumferential boundary as $\Gamma_{\mathrm{C}} = \{(\xi,\alpha)|\xi = 1, \alpha_o \le \alpha \le \alpha_o + \beta\}$. The Γ_{C} condition will be specified later in Section 2.4. Herein, an eigenanalysis of the governing equation and the Γ_{R} condition is concerned.

In the search for the eigenspace, S_l can be divided into two components, S_l^{h} and S_l^{p}, based on the condition given by Eq.(2.5). S_l^{h} represents the homogeneous part, while S_l^{p} represents the non-homogeneous part. In a general sense, f_{b} is a regular function that represents the normal projection of the body motion, and thus, the resultant S_l^{p} belongs to the H^2 space, regardless of the singularity. The eigenspace of the singularity is manifested in the solution space of S_l^{h}, subject to the homogeneous Γ_{R} condition as $\partial S_l^{\mathrm{h}}/\partial\alpha = 0\big|_{\Gamma_{\mathrm{R}}}$.

2.2 SBFEM approximation to the eigen solutions

The eigenspace for corner singularities in the 2D Laplace equation has been well-known as

$$\left\{\cos\left(\sigma_j\left(\alpha - \alpha_o\right)\right)\cdot \xi^{\sigma_j}\right\}, j \in \mathbb{N} \tag{2.6}$$

where $\sigma_j = j\pi/\beta$ is the jth eigenvalue, and $\cos\left(\sigma_j(\alpha - \alpha_o)\right)\xi^{\sigma j}$ is the eigenfunction for the homogeneous Neumann condition on corner sides. In the case of 2D Laplace problems, any possible S^{h} can be expressed as a linear combination of these eigenfunctions. These eigenfunctions can be obtained by separating variables in the circumference and radiation. However, the same approach does not apply to Eq. (2.3). To the best of our knowledge, there is no reported analytic research

196 regarding the singularities of Eq. (2.3). As an alternative, we propose introducing a test function,
197 $w(\xi,\alpha)$, and consider the weak form of Eq.(2.3), viz.,

198 $$\iint_{\Omega_o} r\nabla w\cdot\nabla S_l^{\mathrm{h}}+\frac{l^2}{r}wS_l^{\mathrm{h}}\mathrm{d}\Omega=\int_{\Gamma_{\mathrm{C}}} rwv_{l,n}^{\mathrm{h}}\mathrm{d}\Gamma \tag{2.7}$$

199 where the boundary condition $\partial S_l^{\mathrm{h}}/\partial n=v_{l,n}^{\mathrm{h}}(\alpha)\big|_{\Gamma_{\mathrm{C}}}$ has excluded the component due to S_l^{p}. $\mathbf{n}$ is
200 the normal unit vector outward Ω_o.

201 Considering that the solutions with respect to α are smooth, a Fourier series ansatz for the
202 circumference is reasonable, i.e., the circumferential approximation can be constructed in terms of
203 the cosine basis, $\cos\left(\sigma_j(\alpha-\alpha_o)\right)$. On the other hand, the radial approximation is currently un-
204 known. Let $b_j(\xi)$ denote the radial basis, such that

205 $$\left\{\cos\left(\sigma_j\left(\alpha-\alpha_o\right)\right)\cdot b_j\left(\xi\right)\right\},\ j\in\mathbb{N} \tag{2.8}$$

206 is formally the basis space to approximate S^{h} as

207 $$S_l^{\mathrm{h}}\approx\hat{S}_l^{\mathrm{h}}\left(\alpha,\xi\right)=\sum_{j=0}^{J\to\infty}c_j\cos\left(\sigma_j\left(\alpha-\alpha_o\right)\right)b_j\left(\xi\right) \tag{2.9}$$

208 where c_j is the projection, and J is the number of the truncation. To simplify the formulation, we
209 express Eq. (2.8) in a linear algebra form:

210 $$\hat{S}_l^{\mathrm{h}}\left(\alpha,\xi\right)=\mathbf{F}\left(\alpha\right)\cdot\mathbf{a}\left(\xi\right), \tag{2.10}$$

211 where $\mathbf{a}(\xi)$ is an assemblage of $a_j(\xi)=c_jb_j(\xi)$ representing the radial variation, referred to as the
212 "radial function." Such a technique, which separates the circumferential and radial variables in the
213 weak form of PDEs, is a central concept of SBFEMs. A difference from conventional SBFEMs is
214 that the circumferential basis, $\mathbf{F}(\alpha)$, is a Fourier spectrum rather than the Lagrangian-interpolation-
215 based shape functions. Essential knowledge of SBFEMs for the 2D Laplace equation can be found
216 in Deeks and Cheng (2003) and Li et al. (2005 a, b). The SBFEM formulation for Eq.(2.7) is briefly
217 introduced as follows.

218 Assuming the test function $w=\mathbf{F}(\alpha)\cdot\ \mathbf{v}(\xi)$ belongs to the same space as the basis and firstly
219 integrating with the circumference, Eq. (2.7) turns into

$$\int_0^1 \mathbf{v}_\xi^{\mathrm{T}}\left(\mathbf{E}_{0,0}+\xi\mathbf{E}_{0,1}\right)\xi\mathbf{a}_\xi+\mathbf{v}^{\mathrm{T}}\left(\mathbf{E}_{2,0}+\xi\mathbf{E}_{2,1}+\xi^2\mathbf{M}\left(\xi\right)\right)\frac{1}{\xi}\mathbf{a}\mathrm{d}\xi=\mathbf{v}^{\mathrm{T}}\cdot\mathbf{q}\big|_{\Gamma_{\mathrm{C}}}, \tag{2.11}$$

where $\mathbf{q}$ represents the flux. At Γ_{C}, $\mathbf{q}$ is defined as

$$\mathbf{q}\big|_{\Gamma_{\mathrm{C}}}=\int_{\alpha_o}^{\alpha_o+\beta}\left(r_o-\varsigma_o\cos\left(\alpha-\alpha_o\right)\right)\mathbf{F}v_n\left(\alpha\right)\varsigma_o\mathrm{d}\alpha\,. \tag{2.12}$$

Some matrices are generated as

$$\begin{cases}\mathbf{E}_{0,0}=r_o\int_{\alpha_o}^{\alpha_o+\beta}\mathbf{F}^{\mathrm{T}}\mathbf{F}\mathrm{d}\alpha\\ \mathbf{E}_{0,1}=-\varsigma_o\int_{\alpha_o}^{\alpha_o+\beta}\cos\left(\alpha-\alpha_o\right)\mathbf{F}^{\mathrm{T}}\mathbf{F}\mathrm{d}\alpha\end{cases}, \tag{2.13}$$

$$\begin{cases}\mathbf{E}_{2,0}=r_o\int_{\alpha_o}^{\alpha_o+\beta}\mathbf{F}_\alpha^{\mathrm{T}}\mathbf{F}_\alpha\mathrm{d}\alpha\\ \mathbf{E}_{2,1}=-\varsigma_o\int_{\alpha_o}^{\alpha_o+\beta}\cos\left(\alpha-\alpha_o\right)\mathbf{F}_\alpha^{\mathrm{T}}\mathbf{F}_\alpha\mathrm{d}\alpha\end{cases}, \tag{2.14}$$

and

$$\mathbf{M}\left(\xi\right)=l^2\int_{\alpha_o}^{\alpha_o+\beta}\frac{\varsigma_o^2}{r_o-\varsigma_o\xi\cos\left(\alpha-\alpha_o\right)}\mathbf{F}^{\mathrm{T}}\mathbf{F}\mathrm{d}\alpha\,. \tag{2.15}$$

Based on the orthogonality of the Fourier spectrum, $\mathbf{E}_{0,0}$ and $\mathbf{E}_{2,0}$ are in diagonal forms:

$$\begin{cases}\mathbf{E}_{0,0}=\frac{1}{2}r_o\beta\mathbf{diag}\left(2,1,1,...\right)\\ \mathbf{E}_{2,0}=\frac{1}{2}r_o\beta\mathbf{diag}\left(0,\sigma_1^2,\sigma_2^2,...\right)\end{cases}. \tag{2.16}$$

Taking a Taylor expansion, $\mathbf{M}(\xi)$ is explicitly expressed as

$$\mathbf{M}\left(\xi\right)=\mathbf{M}_0+\xi\mathbf{M}_1+\xi^2\mathbf{M}_2+...\,, \tag{2.17}$$

where the expansion constants read

$$\mathbf{M}_k=l^2\int_{\alpha_o}^{\alpha_o+\beta}\frac{\varsigma_o^{k+2}}{r_o^{k+1}}\cos^k\left(\alpha-\alpha_o\right)\mathbf{F}^{\mathrm{T}}\mathbf{F}\mathrm{d}\alpha\,. \tag{2.18}$$

Performing integrating $\boldsymbol{\omega}_\xi$ by parts and subsequently eliminating $\boldsymbol{\omega}$ due to its arbitrariness, Eq. (2.11) is reformed into a matrix ordinary differential equation (ODE), alias the SBFEM equation, as

$$\left(\mathbf{E}_{0,0}+\xi\mathbf{E}_{0,1}\right)\xi^2\mathbf{a}_{\xi\xi}+\left(\mathbf{E}_{0,0}+2\xi\mathbf{E}_{0,1}\right)\xi\mathbf{a}_\xi-\left(\mathbf{E}_{2,0}+\xi\mathbf{E}_{2,1}+\xi^2\mathbf{M}\left(\xi\right)\right)\mathbf{a}=0\,. \tag{2.19}$$

The flux is represented as a derivative of $\mathbf{a}$

$$\mathbf{q} = \left(\mathbf{E}_{0,0} + \xi\mathbf{E}_{0,1}\right)\xi\mathbf{a}_{\xi}, \tag{2.20}$$

such that $\mathbf{q}(\xi = 1) = \mathbf{q}|_{\Gamma_C}$ should be satisfied.

Eq. (2.19) is solved in the phase space as

$$\boldsymbol{\chi}'(\xi) = \mathbf{H}(\xi)\cdot\boldsymbol{\chi}(\xi), \tag{2.21}$$

where $\boldsymbol{\chi}(\xi) = \left(\mathbf{a}(\xi), \mathbf{q}(\xi)\right)^{\mathrm{T}}$ and the state-transition matrix is

$$\mathbf{H}(\xi) = \xi^{-1}\begin{bmatrix} & \left(\mathbf{E}_{0,0} + \xi\mathbf{E}_{0,1}\right)^{-1} \\ \mathbf{E}_{2,0} + \xi\mathbf{E}_{2,1} + \xi^2\mathbf{M} & \end{bmatrix}. \tag{2.22}$$

$\mathbf{H}(\xi)$ is expanded as a Laurent series with a simple pole at $\xi = 0$:

$$\mathbf{H}(\xi) = \xi^{-1}\sum_{i=0}\xi^i\mathbf{H}_i, \tag{2.23}$$

where the residue $\mathbf{H}_0$ is Hamiltonian as

$$\mathbf{H}_0 = \begin{bmatrix} & \mathbf{E}_{0,0}^{-1} \\ \mathbf{E}_{2,0} & \end{bmatrix}. \tag{2.24}$$

In this first-order linear system with a dimension of $2J + 2$, the vector function $\boldsymbol{\chi}(\xi)$ can be any linear combination of the linearly-independent basis functions, $\boldsymbol{\omega}_j(\xi)$. The indexed matrix $\mathbf{W}(\xi) = \left[\boldsymbol{\omega}_1(\xi), \cdots, \boldsymbol{\omega}_{2J+2}(\xi)\right]$ is, namely, a fundamental space for SBFEM equations. In typical applications of SBFEMs, such as the Laplace problem and the steady/transient elastic problems, $\mathbf{H}(\xi) = \xi^{-1}\mathbf{H}_0$, resulting in a straightforward form for $\mathbf{W}(\xi)$ as $\xi^{\mathbf{H}_0}$. However, in this case, the state-transition matrix is complicated that poses a significant challenge. This issue will be further specified in Section 2.3.

2.3 Fundamental space of the SBFEM for the singularity at an edge

Based on linear algebra, half of the eigenvalues of $\mathbf{H}_0$ are in line with the corner eigenvalues, σ_j, and the other half corresponds to $-\sigma_j$. For ease of later construction, we denote by λ_j the eigenvalues of $\mathbf{H}_0$, and sort them with descending real parts. The mapping between the sets $\{\lambda\}$ and

$\{\sigma\}$ is presented in Table 1, and for convenient reference, we note by j^* the indicators such that $\lambda_{j^*} = \sigma_j$. Each indexed eigenvector is composed of two non-zero elements as

$$\mathbf{t}_{j^*} = \left\{\cdots, 1, \cdots, \sigma_j, \cdots\right\}^{\mathrm{T}} \tag{2.25}$$

where 1 and σ_j are at the $(j+1)$th and $(J+j+2)$th positions.

Table 1 Map between the SBFEM eigenvalues and the corner eigenvalues

λ_1	λ_2	$\cdots$	λ_{J+1}	λ_{J+2}	$\cdots$	λ_{2J+1}	λ_{2J+2}
σ_J	σ_{J-1}	$\cdots$	σ_0	$-\sigma_0$	$\cdots$	$-\sigma_{J-1}$	$-\sigma_J$

The case of $\mathbf{H}(\xi) = \xi^{-1}\left(\mathbf{H}_0 + \xi^2\mathbf{H}_2\right)$ has been specified by Song (1998). The theoretical basics are detailed in Gantmacher (Section 10, Chapter 14, 1959) for a general purpose. In summary, the fundamental space is formed in

$$\mathbf{W}(\xi) = \mathbf{U}(\xi)\mathbf{T}\xi^{\mathbf{\Lambda}}\xi^{\mathbf{L}} \tag{2.26}$$

where $\mathbf{T} = \left[\mathbf{t}_1, \cdots, \mathbf{t}_{2J+2}\right]$ are the indexed eigenvectors of $\mathbf{H}_0$ and $\mathbf{\Lambda} = \mathrm{diag}\left[\lambda_1, \cdots, \lambda_{2J+2}\right]$ the eigenvalues. $\mathbf{U}(\xi)$ and $\mathbf{L}$ are to be determined.

$\mathbf{U}(\xi)$ is constructed as a regular identity at $\xi = 0$ such that

$$\mathbf{U}(\xi) = \mathbf{I} + \xi\mathbf{U}_1 + \xi^2\mathbf{U}_2 + \cdots. \tag{2.27}$$

$\mathbf{L}$ is an upper matrix with zero values on the diagonal. The term of $\xi^{\mathbf{L}} = \mathrm{e}^{\mathbf{L}\ln\xi} = \sum_{i=0}\mathbf{L}^i\ln\xi^i/i!$ leads to the logarithmic polynomials in SBFEM fundamentals. The determination of $\mathbf{U}_i$ and $\mathbf{L}$ can be cumbersome but is accessible by following the matrix ODE theory as detailed in Gantmacher (1959).

We categorize the construction of $\mathbf{U}(\xi)$ and $\mathbf{L}$ in three cases. With increasing complexity, the algorithms are specified as follows:

***Case* 1**: if $\mathbf{H}(\xi) = \xi^{-1}\mathbf{H}_0$, $\mathbf{L}$ is the standard Jordan form of $\mathbf{H}_0$ excluding the diagonal elements, viz., $\mathbf{L} = \mathbf{J} - \mathbf{\Lambda}$, where $L_{i,j} = 0$ except for $L_{J+1,J+2} = 1$. Furthermore, $\mathbf{U}(\xi)$ is the identity constant;

***Case* 2**: if $\mathbf{H}(\xi)$ is multiple, but no eigenvalue differs by an integer, $\mathbf{L}$ equals $\mathbf{J} - \mathbf{\Lambda}$ as in the former case. $\mathbf{U}_i \cdot \mathbf{T} = \left[\overline{\boldsymbol{u}}_1^i, \overline{\boldsymbol{u}}_2^i, \cdots, \overline{\boldsymbol{u}}_{2J+2}^i\right]$ where $\overline{\boldsymbol{u}}_j^i$ is a vector subject to the recurrences:

$$\left(\lambda_j + i - \mathbf{H}_0\right)\bar{\mathbf{u}}_j^i = \begin{cases} 0 & ,i = 0 \\ \sum_{k=1}^{i} \mathbf{A}_k \bar{\mathbf{u}}_j^{i-k} & ,i \geq 1 \end{cases}, \text{ for } j \neq J+2, \tag{2.28}$$

and

$$\left(\lambda_j + i - \mathbf{H}_0\right)\bar{\mathbf{u}}_j^i = \begin{cases} -\bar{\mathbf{u}}_J^i & ,i = 0 \\ \sum_{k=1}^{i} \mathbf{H}_k \bar{\mathbf{u}}_j^{i-k} - \bar{\mathbf{u}}_J^i & ,i \geq 1 \end{cases}, \text{ for } j = J+2. \tag{2.29}$$

***Case* 3**: if $\mathbf{H}(\xi)$ is multiple and some eigenvalues have integer differences, $\mathbf{L}$ is not priorly known, and the recurrence for $\mathbf{U}_i$ can be singular. To handle such a situation, we propose an adjustable recurrence as follows:

$$\left(\lambda_j + i - m_j - \mathbf{A}_0\right)\bar{\mathbf{u}}_j^i = \begin{cases} -\sum_{k=1}^{j-1} L_{k,j} \bar{\mathbf{u}}_k^i & ,i = m_j \\ \sum_{k=1}^{i-m_j} \mathbf{H}_k \bar{\mathbf{u}}_j^{i-k} - \sum_{k=1}^{j-1} L_{k,j} \bar{\mathbf{u}}_k^i & ,i \geq m_j + 1 \end{cases}, \tag{2.30}$$

where $-m_j \geq 0$ is the maximum integer difference between λ_j and the previous eigenvalues. When $\lambda_j + i - m_j$ coincides with another $\lambda_{j'}$, the left-hand side of Eq. (2.30) remains singular, but the equation is solvable by assigning proper values to $L_{i,j}$. By recurrence, all the elements of $L_{i,j}$ and $\bar{\boldsymbol{u}}_j^i$ can be determined, and $\mathbf{U}_i \cdot \mathbf{T} = \left[\bar{\boldsymbol{u}}_1^{i+m_1}, \bar{\boldsymbol{u}}_2^{i+m_2}, \cdots, \bar{\boldsymbol{u}}_{2J+2}^{i+m_{2J+2}}\right]$.

At this point, the SBFEM fundamental space is explicitly defined and will be applied to construct the approximation basis for the corner analysis. The phase-field solution can be chosen from any element in the fundamental space as

$$\boldsymbol{\chi}(\xi) = \mathbf{U}(\xi)\mathbf{T}\xi^{\boldsymbol{\Lambda}}\xi^{\mathbf{L}}\mathbf{C}, \tag{2.31}$$

where $\mathbf{C}$ can be an arbitrary constant vector. Blocking the matrices and vectors in half yields

$$\begin{pmatrix} \mathbf{a}(\xi) \\ \mathbf{q}(\xi) \end{pmatrix} = \mathbf{U}(\xi)\mathbf{T}\begin{bmatrix} \xi^{\boldsymbol{\Lambda}_+}\left(\xi^{\mathbf{L}}\right)_{11} & \xi^{\boldsymbol{\Lambda}_+}\left(\xi^{\mathbf{L}}\right)_{12} \\ & \xi^{\boldsymbol{\Lambda}_-}\left(\xi^{\mathbf{L}}\right)_{22} \end{bmatrix}\begin{pmatrix} \mathbf{c}_1 \\ \mathbf{c}_2 \end{pmatrix}, \tag{2.32}$$

where $(\cdot)_{11}$, $(\cdot)_{12}$, $(\cdot)_{21}$, and $(\cdot)_{22}$ denotes, respectively, the upper-left, upper-right, lower-left, and lower-right blocks of a matrix. Particularly, $\boldsymbol{\Lambda}_+$ and $\boldsymbol{\Lambda}_-$ are, respectively, the non-negative and non-positive blocks of the diagonal $\boldsymbol{\Lambda}$.

$\mathbf{c}_2$ must be zero to vanish the negative exponents $\xi^{\boldsymbol{\Lambda}_-}$ at $\xi = 0$. The radial function is finally

formed in

$$\mathbf{a}(\xi)=\left(\mathbf{U}(\xi)\mathbf{T}\right)_{11}\xi^{\mathbf{\Lambda}_+}\left(\xi^{\mathbf{L}}\right)_{11}\mathbf{c}_1=\mathbf{W}_{11}(\xi)\cdot\mathbf{c}_1, \tag{2.33}$$

and the flux

$$\mathbf{q}(\xi)=\left(\mathbf{U}(\xi)\mathbf{T}\right)_{21}\xi^{\mathbf{\Lambda}_+}\left(\xi^{\mathbf{L}}\right)_{11}\mathbf{c}_1=\mathbf{W}_{21}(\xi)\cdot\mathbf{c}_1. \tag{2.34}$$

So we have found a complete picture of the local velocity potential S_l^{h} under the SBFEM representation. Plugging Eq.(2.33) into Eq.(2.10), and discarding the logarithms, Eq. (2.35) offers a glimpse into the edge singularity:

$$\begin{aligned}\hat{S}_l^{\mathrm{h}}(\xi,\alpha)&=c_{0^*}\left(1+\xi P_0(\xi)\right)+\sum_{j=1}^{J}c_{j^*}\xi^{\sigma_j}\cos\left(\sigma_j(\alpha-\alpha_o)\right)\left(1+\xi P_j(\xi)\right)\\&=c_{0^*}+c_{1^*}\xi^{\sigma_1}\cos\left(\sigma_1(\alpha-\alpha_o)\right)+O\left(\xi+\xi^{\sigma_j+1}\right)\end{aligned}, \tag{2.35}$$

where $P_j(\xi)$ is a regular polynomial as the arrangement of the j^*th column of $\mathbf{U}(\xi)$, and c_{j^*} the element in $\mathbf{c}_1$.

Eq. (2.35) indicates that the basis of a 3D edge can be constructed by the 2D corner basis multiplying polynomials. The herein obtained basis can be viewed as a set of approximated eigenfunctions in the application. It is straightforward to comprehend that for some common structures, such as cylinders and discs, their singular natures are $\xi^{2/3}$ and $\xi^{1/2}$, respectively.

2.4 Determination of the local solutions

Extended from Section 2.1, our focus is to refine the local BVP for S_l. We have already fulfilled the requirements of the Γ_{R} condition through the particular solution S_l^{p}. Now we proceed to define and address the general conditions on Γ_{C}. To distinguish quantities at $\xi=1$, a tilde '$\sim$' is introduced to them.

Dirichlet condition, namely, $\tilde{S}_l=\mathcal{D}(\alpha),\alpha\in[\alpha_o,\alpha_o+\beta]$. The first step is to calculate the expansion coefficients on Γ_{C}, viz., $\tilde{\mathbf{a}}$, as

$$a_j\big|_{\xi=1}=\frac{1}{\beta}\int_{\alpha_o}^{\alpha_o+\beta}\cos^2\left(\sigma_j(\alpha-\alpha_o)\right)\left(\mathcal{D}(\alpha)-\tilde{S}_l^{\mathrm{p}}(\alpha)\right)\mathrm{d}\alpha\begin{cases}1, j=0\\2, j\geq 1\end{cases}. \tag{2.36}$$

By inverting Eq.(2.33), the local problem is solved as

$$S_l^{\mathrm{h}}\left(\xi,\alpha\right)=\mathbf{F}\left(\alpha\right)\cdot\mathbf{a}\left(\xi\right)=\mathbf{F}\left(\alpha\right)\cdot\left(\mathbf{W}_{11}\left(\xi\right)\tilde{\mathbf{W}}_{11}^{-1}\cdot\tilde{\mathbf{a}}\right). \tag{2.37}$$

Neumann condition, namely, $\partial\tilde{S}_l/\partial n=\mathcal{N}(\alpha),\alpha\in[\alpha_o,\alpha_o+\beta]$. By eliminating $\mathbf{c}_1$ in Eq. (2.33) and Eq. (2.34), the relation between $\tilde{\mathbf{a}}$ and $\tilde{\mathbf{q}}$ is

$$\tilde{\mathbf{K}}\cdot\tilde{\mathbf{a}}=\tilde{\mathbf{q}}, \tag{2.38}$$

where

$$\tilde{\mathbf{K}}=\tilde{\mathbf{W}}_{21}\tilde{\mathbf{W}}_{11}^{-1} \tag{2.39}$$

is understood as the stiffness of the SBFEM. Substituting $\tilde{\mathbf{q}}$ with

$$\tilde{\mathbf{q}}=\int_{\alpha_o}^{\alpha_o+\beta}\tilde{r}\left(\alpha\right)\mathbf{F}^{\mathrm{T}}\left(\alpha\right)\left(\mathcal{N}\left(\alpha\right)-\frac{\partial\tilde{S}_l^{\mathrm{p}}}{\partial n}\right)\varsigma_o\mathrm{d}\alpha \tag{2.40}$$

produces $\tilde{\mathbf{a}}$, and again, Eq. (2.37) is usable. In this case, the stiffness is deficient in rank by 1, leading the calculated velocity potential to differ by an arbitrary constant.

Robin condition, namely, $\partial\tilde{S}_l/\partial n=\mathcal{R}(\alpha)S_l+\mathcal{N}(\alpha),\alpha\in[\alpha_o,\alpha_o+\beta]$. By substituting $\tilde{\mathbf{q}}$ with

$$\begin{aligned}\tilde{\mathbf{q}}&=\int_{\alpha_o}^{\alpha_o+\beta}\tilde{r}\left(\alpha\right)\mathbf{F}^{\mathrm{T}}\left(\alpha\right)\left(\mathcal{R}\left(\alpha\right)\left(\mathbf{F}\left(\alpha\right)\tilde{\mathbf{a}}+\partial\tilde{S}_l^{\mathrm{p}}\right)+\left(\mathcal{N}\left(\alpha\right)-\frac{\partial\tilde{S}_l^{\mathrm{p}}}{\partial n}\right)\right)\varsigma_o\mathrm{d}\alpha\\&=\tilde{\mathbf{K}}_{\mathcal{R}}\cdot\tilde{\mathbf{a}}+\tilde{\mathbf{f}}_{\mathcal{R}}\end{aligned}, \tag{2.41}$$

$\tilde{\mathbf{a}}$ is determined based on

$$\left(\tilde{\mathbf{K}}-\tilde{\mathbf{K}}_{\mathcal{R}}\right)\cdot\tilde{\mathbf{a}}=\tilde{\mathbf{f}}_{\mathcal{R}}. \tag{2.42}$$

3 Application to linearized radiation problem in the frequency domain

Section 2 has established the foundation for modeling axisymmetric edge singularities. In this section, we demonstrate the practical application by solving a linear radiation problem. As an illustrative example, we primarily consider a floating cylinder, where the edge is parametrized by $\beta = 3/2\pi$ and $\alpha_o = 0$. The cylinder is assumed to undergo oscillation in the heave direction, in which the vertical mean drift force is recognized as sensitive to the singular effect, as highlighted by, e.g., Zhao and Faltinsen (1989) and Newman and Lee (2002). Therefore, the mean drift force and the velocity field will serve as criteria to examine the accuracy of our approach.

The proposed singular representation Eq. (2.10) is not capable of obtaining global solutions. Hence, a reliable global solver is required. Among the various options, the FEM is excluded due to the so-called "coordinate singularity" issue at $r = 0$, which leads to a deficient rank in the final linear algebra, as discussed in Qiu et al. (2012). The BEM is applicable but a bit heavy to implement. The technique can be found in, for instance, Hulme (1983). Instead, we employ the SEM for its accuracy and easy implementation. Two strategies are devised to tackle the global-local problem. The first strategy involves local refinement. We initially utilize the SEM for obtaining global solutions of the potential, irrespective of singularities. Subsequently, we use the SBFEM as a post-procedure to refine the edge neighborhood. The second strategy is an SEM-SBFEM coupled scheme, which simultaneously solves the local problem and the global problem.

3.1 BVP for the linearized radiation problem and pressure integration for the mean drift force

In a linearized model, the computational domain Ω^3 remains fixed regardless of the time variation. As sketched in Fig. 3, Ω^3 is bounded by four surfaces: $\partial\Omega^3 = \partial\Omega_{\mathrm{f}}^3 \cup \partial\Omega_{\mathrm{b}}^3 \cup \partial\Omega_{\mathrm{d}}^3 \cup \partial\Omega_{\mathrm{r}}^3$. The first two are, respectively, the free surface and the body surface at their equilibriums; the latter two are, respectively, the seabed and the radiational boundary in the far field.

Consider a 3D body undergoing a forced oscillation with an amplitude ζ_j, where the subscript $j = 1\sim6$, respectively, denoting the surge, sway, heave, pitch, yaw, and roll. In this context, we

focus on $j = 3$, which corresponds to the heave motion, is considered. When reaching a steady state, the linear heaving potential is represented by $\Phi(\mathrm{x}, t) = \mathrm{Re}\left[\zeta_3 \phi(\mathrm{x}) \mathrm{e}^{-\mathrm{i}\omega t}\right]$, where $\phi(\mathrm{x})$ is the potential in the frequency domain due to an oscillation with unit amplitude, and ω represents the angular frequency. $\phi(\mathrm{x})$ is governed by the 3D Laplace equation and determined by the following boundary conditions:

$$\partial\phi/\partial n = -\mathrm{i}\omega f_3, \text{ on } \partial\Omega_{\mathrm{b}}^3, \tag{3.1}$$

$$\partial\phi/\partial n - v\phi = 0, \text{ on } \partial\Omega_{\mathrm{f}}^3, \tag{3.2}$$

$$\partial\phi/\partial n = 0, \text{ on } \partial\Omega_{\mathrm{d}}^3, \tag{3.3}$$

and

$$\lim_{r\to\infty} \sqrt{r}\left(\partial\phi/\partial n - \mathrm{i}k\phi\right) = 0, \text{ on } \partial\Omega_{\mathrm{r}}^3, \tag{3.4}$$

where k is the wavenumber of linear waves; $v = \omega^2/g$ is the wave number in deep water; g is the gravity acceleration; $f_3 = n_z$ is the forcing term due to the heaving motion.

Following the concept introduced in Section 2.1, problems of an axisymmetric body are studied in cylindrical coordinates. The origin of the system is at the center of the waterplane, and the z-axis is aligned with the central axis of the floating body, pointing vertically upward, as depicted in Fig. 3. Utilizing the dimensional reduction and considering the symmetry of the problem, the heaving radiational potential is θ-independent and expressed as

$$\phi(r, z, \theta) = \phi_0(r, z). \tag{3.5}$$

ϕ_0 is the reduced potential on the generatrix plane. It is subject to the reduced Laplace equation Eq. (2.3), and the boundary conditions hold the same form as in Eq. (3.1), (3.2), (3.3), and (3.4), respectively, on $\partial\Omega_{\mathrm{b}}^2$, $\partial\Omega_{\mathrm{f}}^2$, $\partial\Omega_{\mathrm{d}}^2$, and $\partial\Omega_{\mathrm{r}}^2$, as illustrated in Fig. 4.

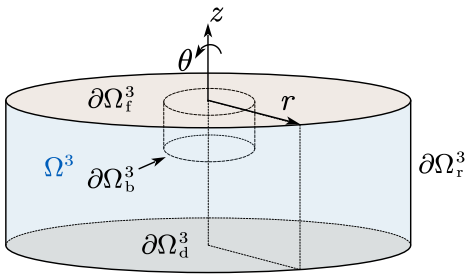

Fig. 3 Sketch of the 3D computational domain

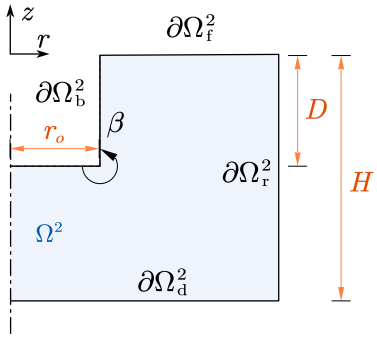

Fig. 4 Dimensional-reduction of the computational domain

The mean drift force, represented as $\mathbf{f}^{\mathrm{m}}$, is calculated via a pressure integration on the body surface using the formulation:

$$\frac{\mathbf{f}^{\mathrm{m}}}{\rho|\zeta_3|^2}=-\frac{1}{4}\iint_{\partial\Omega_{\mathrm{b}}^3}\nabla\phi\cdot\nabla\phi^*\mathbf{n}\mathrm{d}S-\frac{\omega}{2}\iint_{\partial\Omega_{\mathrm{b}}^3}\mathrm{Re}[\mathrm{i}\phi_z^*]\mathbf{n}\mathrm{d}S+\frac{1}{4}\oint_{C_{\mathrm{wp}}}\mathrm{Re}[(v\phi+2\mathrm{i}\omega)]\phi^*\mathbf{n}'\mathrm{d}\Gamma\ , \quad (3.6)$$

where ρ is the fluid density; $C_{\mathrm{wp}}=\partial\Omega_{\mathrm{f}}^3\cap\partial\Omega_{\mathrm{b}}^3$ is the waterline; $\mathbf{n}'$ is the normal unit vector of C_{wp} on the horizontal plane; $*$ is the conjugate operator. The first term in Eq.(3.6) arises from the square product of gradients in Bernoulli's equation; the second term accounts for the body motion; the third term is a correction to the wave elevation, equaling zero for a cylinder or a submerged body. The first term for body surfaces containing edges is strongly singular; the second is weakly singular. Both terms are integrable for $\beta<2\pi$. In the extreme cases where $\beta=2\pi$, corresponding to a thin circular plate, the quadratic product of velocity introduces a ξ^{-1} kernel to the pressure distribution. The issue on whether this term is integrable requires a rigorous investigation, which is beyond the scope of the current content.

The essential geometry parameters of the presented cylinder are specified here. The water depth is $H=1.0\mathrm{m}$. Of the cylinder, both the radius r_o and the draught D, i.e., $|z_o|$, equal $0.3H$.

3.2 SEM solver and the refinement strategy

For sufficient accuracy, the 6th-order Legendre interpolation is employed within each element. Rectangular spectral elements are used. To circumvent the "coordinate singularity" at $r=0$,

different node arrangements are applied, as depicted in Fig. 5. For elements not connected to the axis, the Legendre-Gauss-Lobatto (LGL) nodes are placed in both directions; for elements connected to the axis on one side, parallel to the axis, the Legendre-Gauss-Radau (LGR) nodes are applied instead of the LGL nodes. This arrangement ensures that no nodes are positioned on the axis.

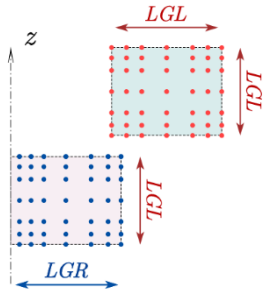

Fig. 5 Node arrangements in spectral elements

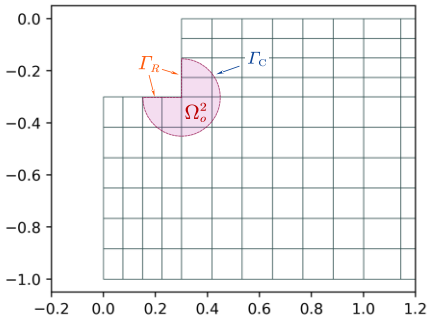

Fig. 6 Mesh-1 for the SEM in the view of near-field; the sector field in pink is refined by the SBFEM

The SEM formulation is

$$\left(\mathbf{K}_{\Omega^2} - v\mathbf{K}_{\partial\Omega_{\mathrm{f}}^2} - \mathrm{i}k\mathbf{K}_{\partial\Omega_{\mathrm{r}}^2}\right)\cdot\boldsymbol{\phi}_l = \mathbf{f}_{\mathrm{b}}, \tag{3.7}$$

where $\boldsymbol{\phi}_l$ is the nodal value vector for ϕ_l. The coefficients are as follows

$$\mathbf{K}_{\Omega^2} = \iint_{\Omega^2} r\nabla\mathbf{N}^{\mathrm{T}}\cdot\nabla\mathbf{N} + \frac{l^2}{r}\mathbf{N}^{\mathrm{T}}\cdot\mathbf{N}\mathrm{d}\Omega, \tag{3.8}$$

$$\mathbf{K}_{\partial\Omega_{\mathrm{f}}^2} = \int_{\partial\Omega_{\mathrm{f}}^2} r\mathbf{N}^{\mathrm{T}}\cdot\mathbf{N}\mathrm{d}\Gamma, \tag{3.9}$$

$$\mathbf{K}_{\partial\Omega_{\mathrm{r}}^2} = \int_{\partial\Omega_{\mathrm{r}}^2} r\mathbf{N}^{\mathrm{T}}\cdot\mathbf{N}\mathrm{d}\Gamma, \tag{3.10}$$

and

$$\mathbf{f}_{\mathrm{b}} = \int_{\partial\Omega_{\mathrm{b}}^2} r\mathbf{N}^{\mathrm{T}} f_3 \mathrm{d}\Gamma\,, \tag{3.11}$$

where **N** is the Legendre-polynomial shape function in the global form.

Structured grids are applied. The basis grid is plotted in Fig. 6, labeled Mesh-1. The elements on the body surface are uniform in size, and the length is notated by $h = r_o/4$. Refinements are made based on the initial Mesh-1 by diminishing the element length to $h/2$ and $h/4$, yielding, namely, Mesh-2 and Mesh-4, respectively. The radius of the corner tip neighborhood remains notated by ς_o.

In the refinement strategy design, the global potential ϕ_l is solved by the SEM. Because the element has small support, the potential outside the edge-neighboring area Ω_o^2 can be accurate. Therefore, we construct a Dirichlet condition on Γ_{C} and solve the local singular filed S_l based on Section 2.4. The particular solution for the present heaving motion is $S_l^{\mathrm{p}} = \mathrm{i}\omega z$.

3.3 Coupling strategy based on the SEM and the SBFEM

The computational domain Ω^2 is divided into Ω_o^2 and $\Omega^2 \backslash \Omega_o^2$. The former region will be modeled using the SBFEM and the latter using the SEM. Γ_{C} is a circular arc with a radius ς_o, serving as the interface to couple the two methods, as illustrated in Fig. 7.

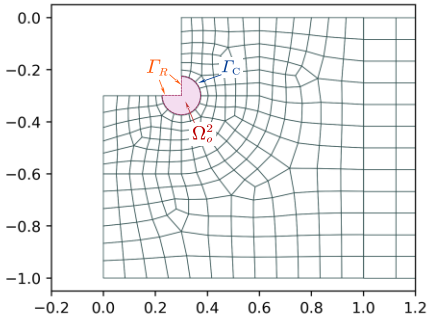

Fig. 7 Mesh for the coupling method in the view of near-field; two methods couple at the interface Γ_{C}; the exemplified radius of Γ_{C} is $\varsigma_o/r_o = 1/4$

The nodal homogenous velocity potentials of the SEM nodes (the nodal number is denoted by M) on Γ_{C} are determined by

$$\left\{\tilde{S}_l^{\mathrm{h}}\right\}=\left\{\mathbf{F}\right\}\cdot\mathbf{a}\left(\xi\right)=\boldsymbol{\psi}\cdot\mathbf{c}_1\,, \tag{3.12}$$

where

$$\boldsymbol{\psi}=\left\{\mathbf{F}\right\}\cdot\tilde{\mathbf{W}}_{11}\,. \tag{3.13}$$

Here, the brace $\{\cdot\}$ notates the nodal vectors for the interface nodes. $\{\mathbf{F}\}=[\mathbf{F}(\alpha_1),\cdots,\mathbf{F}(\alpha_M)]^{\mathrm{T}}$ where $\alpha_{m=1,\ldots,M}$ is the angular coordinate of the mth node.

By taking a generalized inverse of Eq.(3.12), $\mathbf{c}_1$ is estimated by

$$\mathbf{c}_1=\left(\boldsymbol{\psi}^{\mathrm{T}}\boldsymbol{\psi}\right)^{-1}\boldsymbol{\psi}^{\mathrm{T}}\left\{\tilde{S}_l^{\mathrm{h}}\right\}. \tag{3.14}$$

The normal derivative of S_l^{h} on Γ_{C} toward the corner tip is

$$v_{l,n}^{\mathrm{h}}=\frac{\partial\tilde{S}_l^{\mathrm{h}}}{\partial n}=-\frac{1}{\varsigma_o}\mathbf{F}\left(\alpha\right)\tilde{\mathbf{W}}_{11,\xi}\cdot\mathbf{c}_1 \tag{3.15}$$

Substituting Eq.(3.14) into Eq.(3.15) we have

$$v_{l,n}^{\mathrm{h}}=\mathbf{F}\left(\alpha\right)\Theta\cdot\left\{\tilde{S}_l^{\mathrm{h}}\right\} \tag{3.16}$$

where

$$\Theta=-\frac{1}{\varsigma_o}\tilde{\mathbf{W}}_{11,\xi}\left(\boldsymbol{\psi}^{\mathrm{T}}\boldsymbol{\psi}\right)^{-1}\boldsymbol{\psi}^{\mathrm{T}}. \tag{3.17}$$

Finally, we construct the interface relation as

$$\tilde{\mathbf{K}}\Theta\cdot\left\{\tilde{S}_l\right\}=\tilde{\mathbf{f}} \tag{3.18}$$

where

$$\tilde{\mathbf{K}}=\int_{\Gamma_{\mathrm{C}}}r\mathbf{N}^{\mathrm{T}}\cdot\mathbf{F}\mathrm{d}\Gamma\,, \tag{3.19}$$

and

$$\tilde{\mathbf{f}}=\int_{\Gamma_{\mathrm{C}}}r\mathbf{N}^{\mathrm{T}}\tilde{S}_{l,n}^{\mathrm{p}}\mathrm{d}\Gamma-\tilde{\mathbf{K}}\Theta\left\{\tilde{S}_l^{\mathrm{p}}\right\}. \tag{3.20}$$

Plugging Eq.(3.20) into Eq.(3.7), the problem is solved.

4 Results and discussion

4.1 Potentials and velocities on the body surface

To provide a preview of the singularity, the heaving problem of the cylinder is initially solved using a conventional MEEM. Detailed concepts and mathematical formulations can be referred to in Garrett (1971) and Yeung (1981). The distributions of the potential and the weighted tangential derivative, namely, S and $\varsigma^{1/3}S_\tau$, are presented in Fig. 8. In the upper two sub-figures, the variation of S exhibits a noticeable bending at $\varsigma = 0$, where is the corner tip. With an increasing number of expansion terms, S can be considered convergent from a numerical standpoint. However, $\varsigma^{1/3}S_\tau$ is divergent. At the vertical matching interface between the inner and outer subdomains, a Gibbs phenomenon is observed in $\varsigma^{1/3}S_z$, which is an indicator of discontinuity, viz., a singularity.

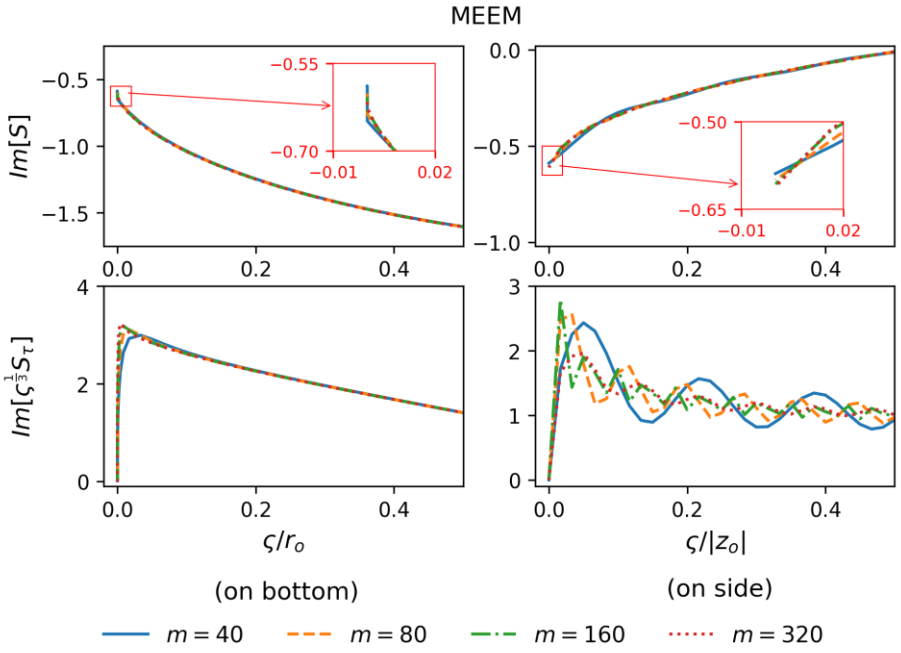

Fig. 8 Potentials and the tangential velocities on the surface of a heaving cylinder by the MEEM; $\omega = 8.0\ \mathrm{rad/s}$; m is truncation number of the MEEM; S_τ refers to S_r and S_z on the bottom and sidewall, respectively; the uppers are the potentials; the lowers are the derivatives

The Gibbs phenomenon, as well as the narrow application, is a major drawback of MEEM. An SEM has no such concern. Hence, we only present the distribution on the bottom, as it is more

characteristic in a heaving problem. As seen in Fig. 9, the SEM exhibits a close agreement with the MEEM in S, and demonstrates rapid convergence as the grid is refined. While investigating $\varsigma^{1/3}S_\tau$, a numerical oscillation is noted in the spectral elements neighboring the corner tip. With finer meshes applied, the oscillation is restrained with smaller magnitudes and bounded in smaller ranges, but the divergence is still as concerning.

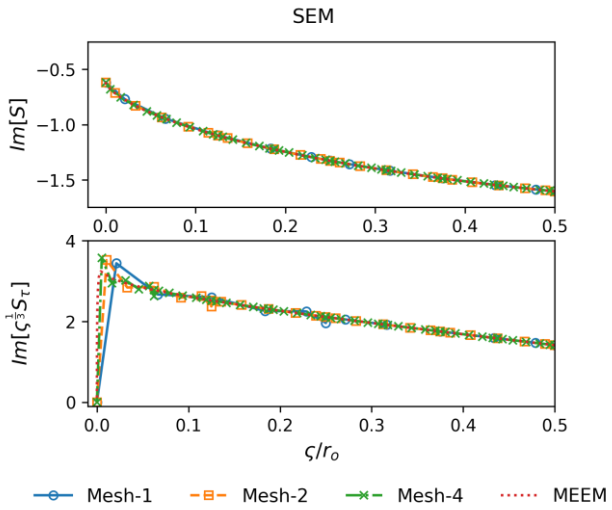

Fig. 9 Potentials and the tangential velocities along the bottom of a heaving cylinder by the SEM; $\omega = 8.0$ rad/s; the scatters denote the nodes; the MEEM is truncated at $m = 320$

In Section 3.2, we conceived a refinement and a coupling strategy. In the refinement strategy, the potentials obtained by the SEM are enforced as the Dirichlet circumferential condition of the refined area Ω_o^2. Subsequently, the SBFEM is applied for singular representation. The radius of the refined area is $\varsigma_o/r_o = 0.5$, and 10 Fourier spectra are applied for circumferential approximation; 20 terms are kept in the SBFEM fundamentals for radial approximation. The results are depicted in Fig. 10. The potential S obtained in the refined area Ω_o^2 shows excellent agreement with the previous MEEM results. This agreement validates the concept that a local singular field could be reconstructed as a post-processing step based on the accurate and reliable boundary quantities away from the singularity. Moreover, when comparing the results of S obtained using the MEEM and the SEM with the more advanced SBFEM, we observe close correspondence. Hence, we can conclude that, even without specific treatment for the singularity, the linear velocity potential can still be easily determined with regular basis functions. However, SBFEMs are particularly distinguished

by their exceptional capability in gradient calculations. The weighted derivative $\varsigma^{1/3}S_\tau$ is now smooth without oscillations, and exhibits notable convergence. The coarse Mesh-1 is considered adequate for accurate gradient estimation. A significant difference can be observed at $\varsigma = 0$. Theoretically, at the edge tip, the nature of the gradient is $\varsigma^{-1/3}$. Hence the weighted gradient $\varsigma^{1/3}S_\tau$ must exhibit a finite value, namely, the stress-intensity factor in fractural mechanics, which typically takes on a non-zero value. The present SBFEM result aligns with this deduction, as the singular nature has been accounted for in Eq. (2.35). However, due to the lack of the SEM and MEEM in the singular basis, finite values can be obtained for S_τ, and thus $\varsigma^{1/3}S_\tau$ jumps to zero at the edge tip.

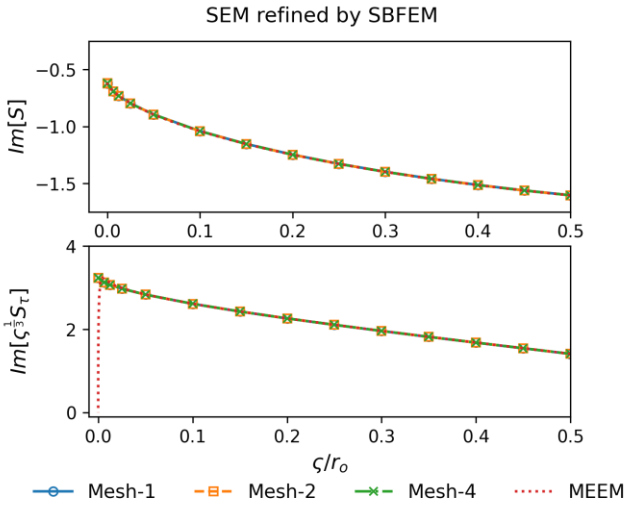

Fig. 10 Potentials and the tangential velocities on the bottom of a heaving cylinder by the refinement strategy; $\omega = 8.0$ rad/s; the MEEM is truncated at $m = 320$

Results obtained using the coupling strategy are presented in Fig. 11. Three unstructured meshes are utilized, with the radii of the coupling interface set to $\varsigma_o/r_o = 1/2$, $1/3$, and $1/4$. The average length of the body-surface elements is $h/r_o = 1/8$, while the element size slightly decreases towards the edge tip to improve the coupling, as exampled in Fig. 7. The potential and velocity variations align with those in Fig. 10, indicating accuracy. Nevertheless, in the vicinity of the coupling interface, the derivatives may exhibit some lack of smoothness. This drawback is addressed by the C_0 continuity of the present scheme. Improving the continuity is possible and under way, but as the discontinuities in velocities do not significantly impact the overall accuracy, this

issue is not urgent in this paper.

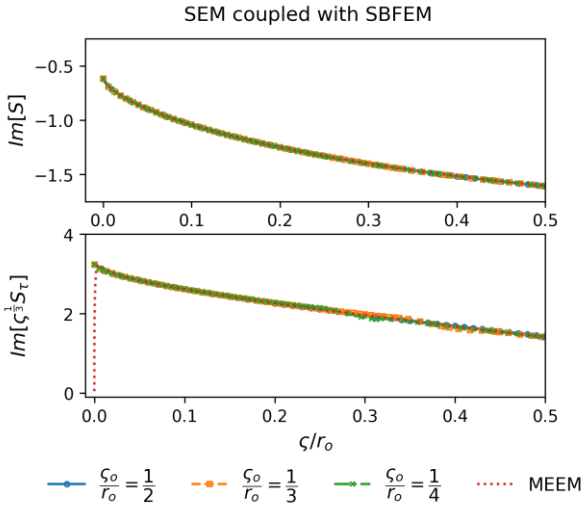

Fig. 11 Potentials and the tangential velocities on the bottom of a heaving cylinder by the coupling strategy; $\omega = 8.0$ rad/s; the scatters denote the nodes; the legends indicate the radii of the coupling interfaces; the MEEM is truncated at $m = 320$.

4.2 Velocity field in the edge neighborhood

The singularity is illustrated in two antitheses groups. Firstly, a singular velocity field will be contrasted with a regular one; secondly, a roughly approximated singular field (by the SEM) will be contrasted with a refined one (by the SBFEM).

Fig. 12 plots the velocity fields of heaving cylinders with rounded and sharp edges. The chamfer radius for the rounded case is $1/6$ of the cylinder radius. The arrows in the figure represent the velocity of the fluid particles; the length and color of the arrows indicate the magnitude. When the cylinder sinks, the water below it is pushed and spreads outwards from the central axis. From Fig. 12(a), it is observed that when the water flow approaches and passes the rounded edge, the downward flow gradually changes direction and eventually flows upward along the sidewall. During this process, there is no significant growth in speed. Whereas the situation is different for a sharp edge, as shown in Fig. 12(b). When tracing a spatial point along the body surface towards the edge tip, as $(r_o - \delta, z_o) \to (r_o, z_o) \to (r_o, z_o + \delta)$, the velocity undergoes a significant change. As the flow

bypasses the sharp edge beneath the bottom, the velocity abruptly turns upward with a steep increase in speed; past the edge tip, the velocity is not vertically upward on the sidewall. In this region, the body surface condition is violated. Moreover, due to the numerical dissipation of spectral elements, the velocity jump at the edge tip is smeared into divergence.

Fig. 13 illustrates the refined velocity field of the sharp edge case using the SBEFM. The SBFEM allows for high-resolution velocity calculations in the immediate vicinity of the edge tip. Fig. 14 depicts the velocity variations along the circumferences at minimal radii for different values of $\varsigma/r_o = 1/20, 1/80, 1/160$ and $1/10000$. Unlike the SEM, the SBFEM strictly adheres to the body condition. As the space point approaches the edge tip beneath the cylinder, i.e., $(r_o - \delta, z_o) \rightarrow (r_o, z_o)$, the orientational angle with respect to the horizontal vanishes, and the velocity tend to parallel to the bottom face, but the vertical projection of the velocity holds due to the body motion. Consequently, the magnitude becomes infinite. The velocity jump at the tip is captured, as it is horizontal before reaching the tip, vertical after passing the tip, and void at the tip itself.

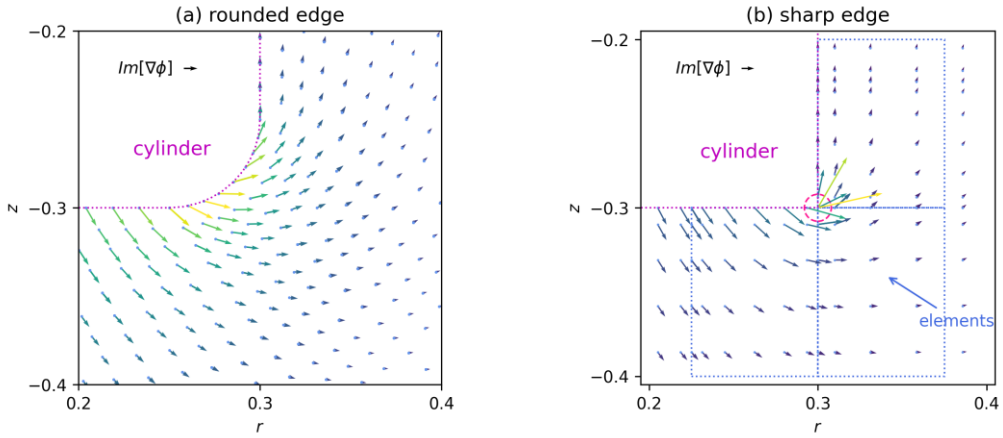

Fig. 12 Velocity field near heaving cylinders with rounded and sharp edges, obtained by the SEM

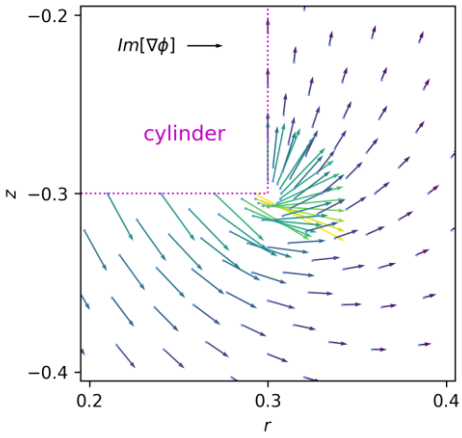

Fig. 13 Velocity field near a heaving cylinder with a sharp edge, obtained by the SBFEM

534

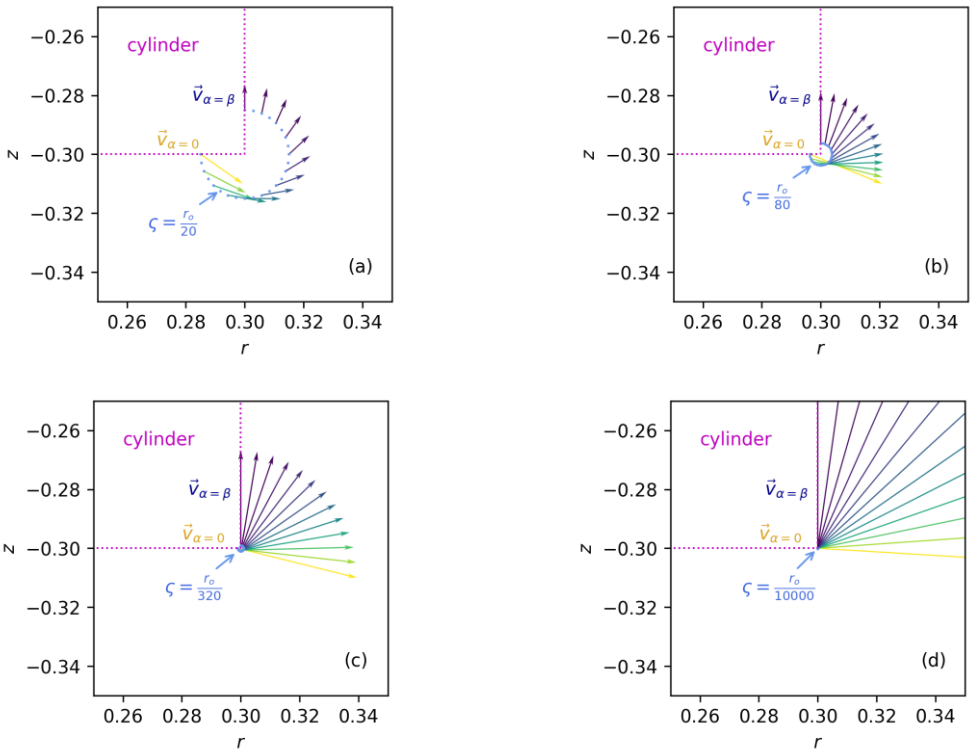

Fig. 14 Velocity variation along circumferences with different radii; a sharp edge case in a heave motion; $\vec{v}_{\alpha=0}$ is the velocity on the bottom, and $\vec{v}_{\alpha=\beta}$ on the sidewall

535 As a reference, following the discussion on the heave motion, here we also present the corre-
536 sponding results under a surge motion, as shown in Fig. 15 and Fig. 16. By comparing Fig. 12 with
537 Fig. 15, it is observed that for a rounded-edge case in the heave motion, the high-velocity point is
538 located at the intersection of the bottom face and the chamfer, while in the surge case, it moves to

the intersection on the sidewall. For the sharp-edge case, the edge tip consistently remains the high-velocity point. But there are still some differences in the cases of the two motions. Referring to Fig. 13 and Fig. 14, it can be seen that in the heave case, the velocity beneath the bottom exhibits a higher magnitude; referring to Fig. 15 and Fig. 16 in the surge case, the situation is reversed. Based on these observations, it can be considered that for a moving body, areas on the body surface that undergo a sudden change in curvature tend to exhibit high-velocity. Among these regions, those that encounter a higher normal flux due to the body motion are likely to have higher fluid velocity in the tangent.

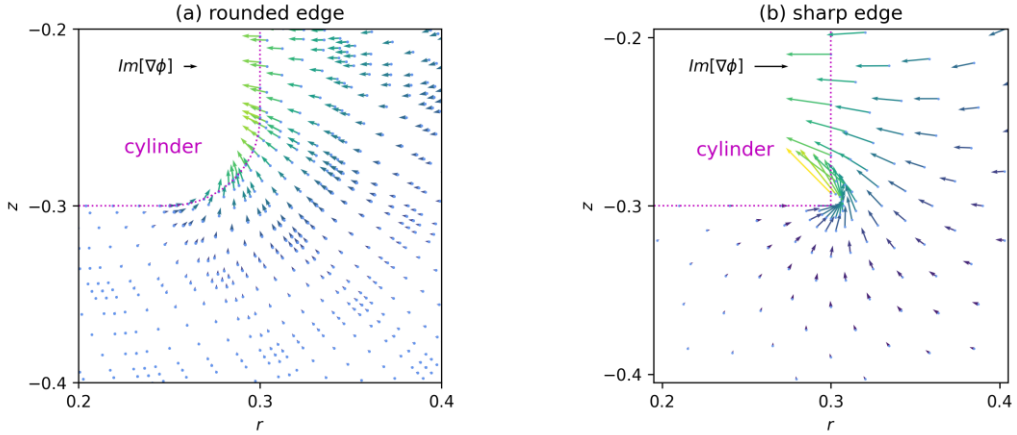

Fig. 15 Velocity field near surging cylinders with rounded and sharp edges, obtained by the SEM and the SBFEM, respectively

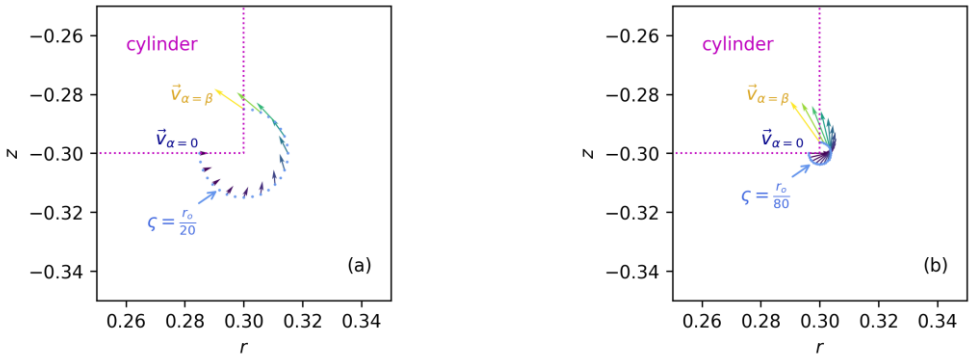

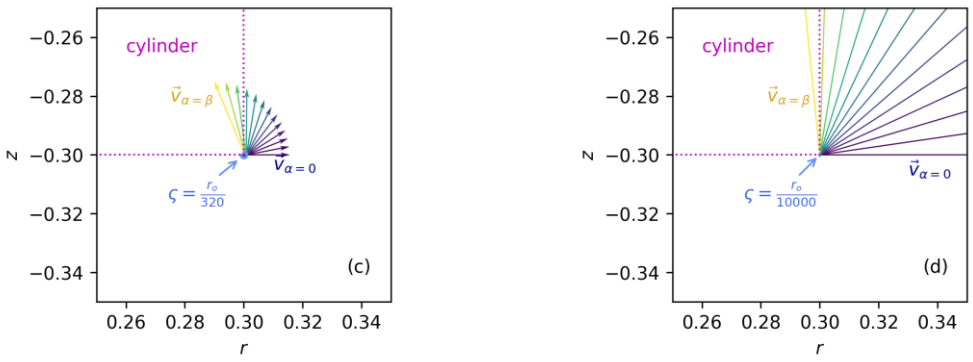

Fig. 16 Velocity variation along circumferences with different radii; a sharp edge case in a surge motion; $\vec{v}_{\alpha=0}$ is the velocity on the bottom, and $\vec{v}_{\alpha=\beta}$ on the sidewall

4.3 Mean drift force under edge effect

Fig. 17 and Fig. 18 show the normalized vertical mean drift force, i.e., $f_z^{\mathrm{m}}/(\rho g r_o |\zeta_3|^2)$ due to the heave motion with respect to the dimensionless wave number vr_o. The results are obtained using the direct pressure integration (Eq. (3.6)). Fig. 17 shows the results by the SEM, while Fig. 18 shows the results by the refinement strategy with a supporting radius of $\varsigma_o/r_o = 0.5$. The SBFEM enables elaborated pressure integration near the edge tip. Both the truncation numbers in the SBFEM fundamentals and the circumferential Fourier basis are set to 10. The middle-field result is included for reference.

From Fig. 17, it can be seen that none of the meshes obtains the correct result. At low frequencies as $\omega \to 0$, results obtained through the direct pressure integration tend to converge to zero; however, as the frequency increases, the divergence becomes more pronounced. This behavior can be explained by referring to Eq. (3.6). In the vicinity of zero frequency, the solutions of the linear velocity potential exhibit a linear dependency on ω. Consequently, the contributions of the three components of the mean drift force become second- and higher-order terms with respect to ω. Errors originating from singularities remain hidden at low frequencies, but become apparent at normal frequencies. From a physical viewpoint, when a floating body moves at an extremely slow speed, a minimal disturbance is induced to the fluid bulk, and the wave elevation is imperceptible. The effect of hydrodynamic pressure has not yet become apparent; hence, the wave forces are

insignificant.

By refining the meshes, the results approach the middle-field results, but significant deviations still persist. Even with extremely dense meshes, the results do not converge. To understand the source of divergence, it is necessary to examine the individual components of Eq.(3.6) in a term-by-term manner. While the third component is zero, the first and second components are presented in Table 2. Both components exhibit similar magnitudes but-in opposite directions. Consequently, the drift force becomes sensitive to these delicate differences. From Table 2, it is observed that the second component converges relatively easily because the weak singular kernel is not pronounced; whereas the first component presents challenges.

In contrast, Fig. 18 demonstrates that with the singularity represented, the near-field result obtained by the refinement strategy exhibits accuracy comparable to the middle-field method. The coupling SEM-SBFEM also achieves equivalent accuracy, as shown in Fig. 19. The selection of the coupling interface has minimal impact on the accuracy.

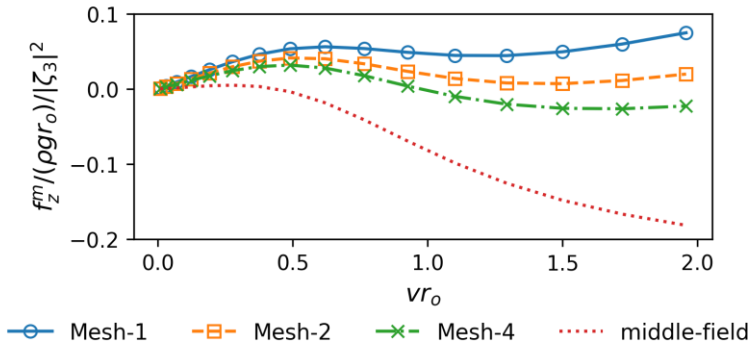

Fig. 17 Vertical mean drift force by the SEM

Table 2 Components of the normalized vertical drift force

a. first component

ω	SEM			refined by SBFEM		
(rad/s)	Mesh-1	Mesh-2	Mesh-4	Mesh-1	Mesh-2	Mesh-4
2.0	-0.1759	-0.1789	-0.1811	-0.1896	-0.1896	-0.1897
4.0	-0.7154	-0.7277	-0.7372	-0.7723	-0.7725	-0.7726
6.0	-1.6854	-1.7161	-1.7399	-1.8277	-1.8283	-1.8285
8.0	-3.0006	-3.0556	-2.9082	-3.2555	-3.2564	-3.2568

b. second component

ω	SEM			refined by SBFEM		
(rad/s)	Mesh-1	Mesh-2	Mesh-4	Mesh-1	Mesh-2	Mesh-4

2.0	0.1922	0.1922	0.1922	0.1922	0.1922	0.1922
4.0	0.7688	0.7688	0.7688	0.7688	0.7688	0.7688
6.0	1.7298	1.7298	1.7299	1.7298	1.7298	1.7298
8.0	3.0753	3.0753	3.0753	3.0753	3.0753	3.0753

581

c. comparison with the middle-field method

ω	SEM			refined by SBFEM			middle-
(rad/s)	Mesh-1	Mesh-2	Mesh-4	Mesh-1	Mesh-2	Mesh-4	field
2.0	0.0163	0.0134	0.0111	0.0026	0.0026	0.0026	0.0026
4.0	0.0534	0.0411	0.0316	-0.0034	-0.0037	-0.0038	-0.0037
6.0	0.0445	0.0138	-0.0100	-0.0979	-0.0984	-0.0986	-0.0988
8.0	0.0747	0.0197	-0.0229	-0.1802	-0.1811	-0.1815	-0.1818

582

583

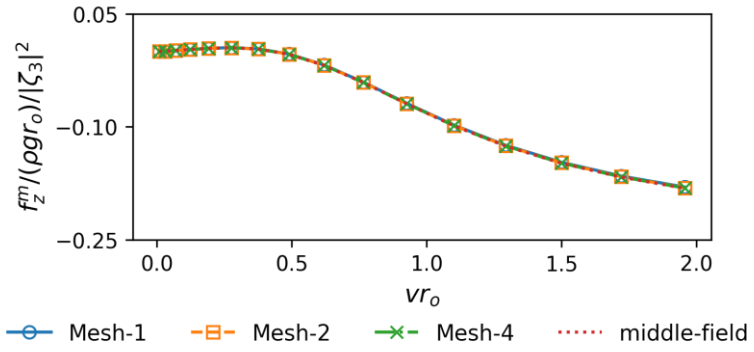

Fig. 18 Vertical mean drift force by the refinement strategy

584

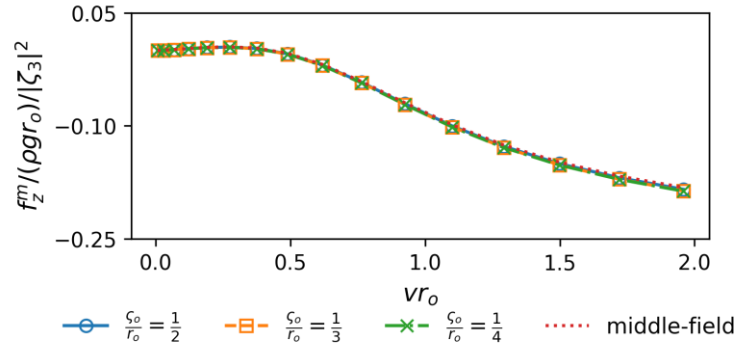

Fig. 19 Vertical mean drift force by the coupling strategy; the legends indicate the radii of the coupling interfaces

585 Furthermore, the influence of singularity on the mean drift force is evaluated by comparing
586 sharp-edge cylinders with rounded-edge cylinders, as shown in Fig. 20. For the rounded-edge cases,
587 very coarse grids ($h/r_o \approx 1/6$) are applied to implement the direct pressure integration, resulting
588 in high agreement with the middle-field method. It is observed that the sharp-edge and rounded-

edge cases closely coincide at low frequencies, indicating that although the sharp edge poses computational challenges, the overall hydrodynamic effect on bodies does not significantly differ from the rounded cases. Since the singular effect is confined to a small range, the inclusion of a singular kernel in the pressure integration leads to a bounded component in the wave forces, assuming accurate calculations are made. This conclusion can be further explained from a physical standpoint: when the body moves slowly, the flow separation manifests as a local phenomenon, causing minor disturbances to the surrounding fluid. Consequently, the overall momentum of the fluid field remains largely unaffected when observed on a macroscopic scale. As a result, the wave forces acting on the structures can be considered approximately equivalent.

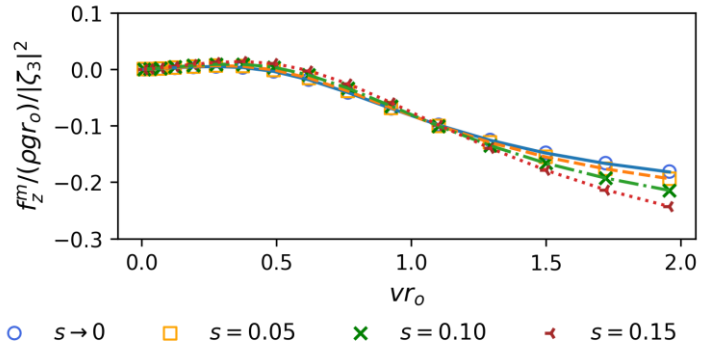

Fig. 20 Effect of chamfer radius of smoothed edge on vertical mean drift force; s is the ratio of the radius of the chamfer to the cylinder; $s \to 0$ represents the sharp edge case; scatters stand for the near-field results and lines stand for the middle-field results

5 Conclusion

This work aims at modeling the singularities present at 3D edges of axisymmetric structures. The 3D problem is dimensionally reduced to the generatrix plane via a circumferential Fourier expansion. However, the reduced governing equation becomes complex and the eigenfunctions of singularities cannot be obtained through conventional methods. To address this, we adopt the SBFEM approach and analyze the weak form instead of the original equation. For the smooth circumferential variation, we employ a cosine spectrum; regarding the singular radial variation, we preserve its singular nature by constructing a matrix ODE and further analytically solving it. The SBFEM fundamentals are of fractional order and serve as the approximation basis for these singularities. We present approaches to address local BVPs with Dirichlet, Neumann, and Robin conditions. A refinement strategy and a coupling strategy are proposed to model both the local singular field and the global field using the SEM and SBFEM solvers. With the numerical method established, we investigate a heaving cylinder as an example and summarize the main findings as follows.

(i) The singular nature at an axisymmetric edge aligns with that at a corner on the generatrix plane, but the eigenfunctions exhibit greater complexity as perturbation expansions based on the 2D corner solutions. In certain cases, some logarithms may arise. In the case of the cylinder example, the edge tip is characterized as producing a $\varsigma^{-1/3}$ singularity in the velocity components, which coincides with a rectangular corner.

(ii) The present semi-analytic analysis allows for the precise determination of velocity in the vicinity of the edge tips. When approaching the edge tip beneath a heaving cylinder, as $(r_o - \delta, z_o) \to (r_o, z_o)$, the orientational angle of the fluid velocity with respect to the horizontal plane vanishes, while the vertical projection maintains accordance with the body motion. Consequently, the velocity magnitude becomes infinite at the tip. Moving upwards along the sidewall, as $(r_o, z_o) \to (r_o, z_o + \delta)$, the velocity becomes purely vertical, satisfying the nonhomogeneous boundary condition. The velocity exhibits a jump at the edge tip, as the present method captures. In contrast, the SEM smears the jump and distorts the representation of the velocity field. Within

the potential flow framework, in a more general scenario involving a moving body, areas on the body surface that undergo a rapid change in curvature tend to exhibit high velocity. And among these regions, those that experience higher normal flux from the body motion are likely to have higher fluid velocity in the tangent.

(iii) The distorted fluid velocity by the SEM results in significant errors in pressure integrations. Specifically, when considering the vertical mean drift force, the integrations of the square product of Bernoulli's equation and the body motion terms have similar magnitudes but opposite directions. When combing them, the mean drift force becomes a delicate quantity that is unlikely to converge using regular approximations. The present method takes exceptional care of the singularities and achieves a level of accuracy and efficiency in direct pressure integration comparable to the middle-field method. To further validate the approach, forces on sharp-edge and rounded-edge cylinders are compared. It is observed that the presence of singularities does not significantly affect the mean drift force when employing the present method.

Acknowledgement

The work was supported by the National Natural Science Foundation of China (No 52271261).

641 **Reference**

642 M. H. Bazyar, A. Talebi, “Scaled boundary finite-element method for solving non-homogeneous
643 anisotropic heat conduction problems,” Appl. Math. Model., 39(23-24), 7583-7599 (2015).
644 https://doi.org/10.1016/j.apm.2015.03.024
645
646 T. Belytschko, T. Black, “Elastic crack growth in finite elements with minimal remeshing,” Int.
647 Numer. Meth. Eng., 45(5), 601-620 (1999).
648 https://doi.org/10.1002/(SICI)1097-0207(19990620)45:5<601::AID-NME598>3.0.CO;2-S
649
650 H. B. Bingham, H. Zhang, “On the accuracy of finite-difference solutions for nonlinear water
651 waves,” J. Eng. Math., 58(1-4), 211-228 (2007).
652 http://doi.org/10.1007/s10665-006-9108-4
653
654 Z. Cai, S. Kim, “A finite element method using singular functions for the Poisson equation: corner
655 singularities,” SIAM J. Numer. Anal., 39(1), 286-299 (2001).
656 https://doi.org/10.1137/S0036142999355945
657
658 Z. Cai, S. Kim, G. Woo, “A finite element method using singular functions for the Poisson equation:
659 crack singularities,” Numer. Linear Algegra Appl., 9(6-7), 445-455 (2002).
660 https://doi.org/10.1002/nla.303

Z. Cai, Seokchan Kim, Sangdong Kim, S. Kong, “A finite element method using singular functions for Poisson equations: mixed boundary conditions,” Comput. Method Appl. M., 195, 2635-2648 (2006).
https://doi.org/10.1016/J.CMA.2005.06.004

A. Chanda, A. Sarkar, S. N. Bora, “An analytical study of scattering of water waves by a surface-piercing bottom-mounted compound porous cylinder placed on a porous sea-bed,” J. Fluids Struct., 115, 103764 (2022).
https://doi.org/10.1016/j.jfluidstructs.2022.103764

K. H. Chang, D. H. Tsaur, L. H. Huang, “Accurate solution to diffraction around a modified V-shaped breakwater,” Coastal Eng., 68, 56-66 (2012).
https://doi.org/10.1016/j.coastaleng.2012.05.002

X. B. Chen, “Middle-field formulation for the computation of wave-drift loads,” J. Eng. Math., 59, 61-82 (2007).
https://doi.org/10.1007/s10665-006-9074-x

H. J. Choi, J. R. Kweon, “The stationary Navier-Stokes system with no-slip boundary condition on

polygons: corner singularity and regularity," Commun. Partial Differ. Equ. 38(7), 1235-1255 (2013).
https://doi.org/10.1080/03605302.2012.752386

H. J. Choi, J. R. Kweon, "A Finite element method for singular solutions of the Navier-Stokes equations on a non-convex polygon," J. Comput. Appl. Math., 292, 432-262 (2016).
https://doi.org/10.1016/j.cam.2015.07.006

P. Cong, B. Teng, L. Chen, Y. Gou, "A novel solution to the second-order wave radiation force on an oscillating truncated cylinder based on the application of control surfaces," Ocean Eng., 204, 107278 (2020).
https://doi.org/10.1016/j.oceaneng.2020.107278

Y. S. Dai, X. B. Chen, W. Y. Duan, "Computation of low-frequency loads by the middle-field formulation," The 20th Int. Workshop on Water Waves and Floating Bodies, Longyearbyen, Norway, 47-50 (2005).

A. Das, S. De, B. N. Mandal, "Radiation of water waves by a heaving submerged disc in a three-layer fluid," J. Fluids Struct., 111, 103575 (2022).
https://doi.org/10.1016/j.jfluidstructs.2022.103575

A. Das, S. De, B. N. Mandal, “Wave interaction with an elliptic disc submerged in a two-layer fluid,” Appl. Math. Model., 117, 786-801 (2023).
https://doi.org/10.1016/j.apm.2023.01.016

A. J. Deeks, L. Cheng, “Potential flow around obstacles using the scaled boundary finite-element method,” Int. Numer. Meth. Fl., 41(7), 721-741 (2003).
https://doi.org/10.1002/FLD.468

R. Eatock Taylor, S. M. Hung, “Second order diffraction forces on a vertical cylinder in regular waves,” Appl. Ocean Res., 9(1), 19-30 (1987).
https://doi.org/10.1016/0141-1187(87)90028-9

A. P. Engsig Karup, H. B. Bingham, O. Lindberg, “An efficient flexible-order model for 3D non-linear water waves,” J. Comput. Phys., 228(6), 2100-2118 (2009).
https://doi.org/10.1016/j.jcp.2008.11.028

L. Farina, R. L. Gama, S. Korotov, J. S. Ziebell, “Radiation of water waves by a submerged nearly circular plate,” J. Comput. Appl. Math., 310, 165-173 (2017).
https://dx.doi.org/10.1016/j.cam.2016.04.009

721

722 R. Gadi, R. H. M. Huijmans, I. Akkerman, B. Veer, “Efficient methodology of roll load prediction
723 on 2D bodies in nonlinear flows,” The 33rd Int. Workshop on Water Waves and Floating Bodies,
724 Brest, France, 4-7 April (2018).

725

726 F. R. Gantmacher, “The theory of matrices,” Vol. 2, Chelsea, New York (1977).

727

728 C. J. R. Garrett, “Wave forces on a circular dock,” J. Fluid Mech., 46(1), 129-139 (1971).
729 https://doi.org/10.1017/S0022112071000430

730

731 F. C. Hanssen, G. Greco, “A potential flow method combining immersed boundaries and overlap-
732 ping grids: formulation, validation and verification,” Ocean Eng., 227, 108841 (2021).
733 https://doi.org/10.1016/j.oceaneng.2021.108841

734

735 S. Hell, W. Becker, “An enriched scaled boundary finite element method for 3D cracks,” Eng. Fract.
736 Mech., 215,272-293 (2019).
737 https://doi.org/10.1016/j.engfracmech.2019.04.032

738

739 A. Hulme, “A ring-source/integral-equation method for the calculation of hydrodynamic forces ex-
740 erted on floating bodies of revolution,” J. Fluid Meth., 128, 387-412 (1983).

https://doi.org/10.1017/S002211208300052X

M. Kashiwagi, T. Momoda, M. Inada, “A time-domain nonlinear simulation method for wave-induced motions of a floating body,” J. Soc. Nav. Arct. JPN., 1998(184),139-148 (1998).
https://doi.org/10.2534/jjasnaoe1968.1998.184_139

M. H. Kim, D. K. P. Yue, “The complete second-order diffraction solution for an axisymmetric body, Part 1. Monochromatic incident waves,” J. Fluid, Mech., 200, 235-264 (1989).
https://doi.org/10.1017/S0022112089000649

M. H. Kim, D. K. P. Yue, “The complete second-order diffraction solution for an axisymmetric body, Part 2. Bichromatic incident waves and body motions,” J. Fluid, Mech., 211, 557-593 (1990).
https://doi.org/10.1017/S0022112090001690

C. H. Lee, “On the evaluation of quadratic forces on stationary bodies,” J. Eng. Math. 58, 141–148 (2007).
https://doi.org/10.1007/s10665-006-9111-9

A. J. Li, Y. Liu, H. J. Li, “New analytical solutions to water wave radiation by vertical truncated cylinders through multi-term Galerkin method,” Meccanica, 54(3), 429-450 (2019).

https://doi.org/10.1007/s11012-019-00964-x

A. J. Li, Y. Liu, “New analytical solutions to water wave diffraction by vertical truncated cylinders,” Int. J. Nav. Arch. Ocean, 11(2), 952-969 (2019).
https://doi.org/10.1016/j.ijnaoe.2019.04.006

B. Li, L. Cheng, A. J. Deeks, B. Teng, “A modified scaled boundary finite-element method for problems with parallel side-faces. Part II. Application and evaluation,” Appl. Ocean Res., 27, 224-234 (2005).
https://doi.org/10.1016/j.apor.2005.11.007

B. Li, L. Cheng, A. J. Deeks, B. Teng, “A modified scaled boundary finite-element method for problems with parallel side-faces. Part I. Theoretical developments,” Appl. Ocean Res., 27, 216-223 (2005).
https://doi.org/10.1016/j.apor.2005.11.008

H. Liang, O. M. Faltinsen, Y. L. Shao, “Application of a 2D harmonic polynomial cell (HPC) method to singular flows and lifting problems,” Appl. Ocean Res., 53, 75-90 (2015).
http://dx.doi.org/10.1016/j.apor.2015.07.011

781 H. Liang, S. Zheng, Y. Shao, K. H. Chua, Y. S. Choo, D. Greaves, “Water wave scattering by im-
782 permeable and perforated plates,” Phys. Fluids, 33, 077111 (2021).
783 http://doi.org/10.1063/5.0051355
784
785 J. Lighthill, “Waves and hydrodynamic loading,” Proc. of the Second Int. Conf. on Behavior of
786 Offshore Structures, London, 1979: 1:1-40, (1979).
787
788 X. Y. Long, C. Jiang, X. Han, W. Gao, R. G. Bi, “Sensitivity analysis of the scaled boundary finite
789 element method for elastostatics,” Comput. Methods Appl. Mech. Engrg., 276(2014), 212-232
790 (2014).
791 http://dx.doi.org/10.1016/j.cma.2014.03.005
792
793 Q. W. Ma, G. X. Wu, R. Eatock Taylor, “Finite element simulation of fully non-linear interaction
794 between vertical cylinder and steep waves. Part 1: methodology and numerical procedure,” Int. J.
795 Numer. Meth. Fl., 36(3), 265-285 (2001).
796 https://doi.org/10.1002/fld.131
797
798 Q. W. Ma, G. X. Wu, R. Eatock Taylor, “Finite element simulation of fully non-linear interaction
799 between vertical cylinder and steep waves. Part 2: numerical results and validation,” Int. J. Numer.
800 Meth. Fl., 36(3), 287-308 (2001).

https://doi.org/10.1002/fld.133

H. Martins Rivas, C. C. Mei, “Wave power extraction from an oscillating water column at the tip of a breakwater,” J. Fluid Mech., 626, 395-414 (2009).
https://doi.org/10.1017/S0022112009005990

P. A. Martin, S. G. Llewellyn Smith, “Generation of internal gravity waves by an oscillating horizontal disc,” Proc. R. Soc. A, 467, 3406-3423 (2011).
https://doi.org/10.1098/rspa.2011.0193

B. Molin, “Second-order diffraction loads upon three dimensional bodies,” Appl. Ocean Res., 1, 197-202 (1979).
https://doi.org/10.1016/0141-1187(79)90027-0

J. N. Newman, C. H. Lee, “Boundary-element methods in offshore structure analysis,” J. Offshore Mech. Arct. Eng., 124(2), 81-89 (2002).
https://doi.org/10.1115/1.1464561

R. Porter, “Linearised water wave problems involving submerged horizontal plates,” Appl. Ocean Res., 50, 91-109 (2015)

http://dx.doi.org/10.1016/j.apor.2014.07.013

R. Porter, D. V. Evans, “Complementary approximations to wave scattering by vertical barriers,” J. Fluid Mech., 294, 155-180 (1995).
https://doi.org/10.1017/S0022112095002849

Z. Qiu, Z. Zeng, H. Mei, L. Li, L. Yao, L. Zhang, “A Fourier-Legendre spectral element method in polar coordinates,” J. Comput. Phys. 231, 666-675 (2012).
https://doi.org/10.1016/j.jcp.2011.10.003

A. Sarkar, A. Chanda, “Structural performance of a submerged bottom-mounted compound porous cylinder on the water wave interaction in the presence of a porous sea-bed,” Phys. Fluids, 34, 092113 (2022).
https://doi.org/10.1063/5.0106425

P. D. Sclavounos, “Nonlinear impulse of ocean waves on floating bodies,” J. Fluid Mech., 697, 316-337 (2012).
https://doi.org/10.1017/jfm.2012.68

Y. L. Shao, O. M. Faltinsen, “A harmonic polynomial cell (HPC) method for 3D Laplace equation

841 with application in marine hydrodynamics," J. Comput. Phys., 274, 312-332 (2014).
842 https://doi.org/10.1016/j.jcp.2014.06.021
843
844 Y. L. Shao, O. M. Faltinsen, "Fully-nonlinear wave-current-body interaction analysis by a harmonic
845 cell method," J. Offshore Mech. Arct. Eng., 136(3), 031301 (2014).
846 https://doi.org/10.1115/1.4026960
847
848 Y. L. Shao, O. M. Faltinsen, "Towards efficient fully-nonlinear potential-flow solvers in marine
849 hydrodynamics," Int. Conf. Ocean Offshore Arct. Eng., OMAE, 2012-83319, 369-380 (2012).
850 https://doi.org/10.1115/OMAE2012-83319
851
852 C. Song, J. P. Wolf, "The scaled boundary finite-element method alias consistent infinitesimal finite
853 element cell method for elastodynamics," Comput. Method Appl. M., 147(3-4), 329-355 (1997)
854 https://doi.org/10.1016/S0045-7825(97)00021-2
855
856 C. Song, J. P. Wolf, "The scaled boundary finite-element method: analytical solution in frequency
857 domain," Comput. Method Appl. M., 164, 249-264 (1998).
858 https://doi.org/10.1016/S0045-7825%2898%2900058-9
859
860 C. Song, J. P. Wolf, "The scaled boundary finite-element method - a primer: solution procedures,"

Comput. Struct., 78(1-3), 211-225 (2000).
https://doi.org/10.1016/S0045-7949(00)00100-0

C. Song, “A matrix function solution for the scaled boundary finite-element equation in statics,” Comput. Method Appl. M., 193, 2325-2356 (2004).
https://doi.org/10.1016/J.CMA.2004.01.017

L. Tao, H. Song, S. Chakrabarti, “Scaled boundary FEM solution of short-crested wave diffraction by a vertical cylinder,” Comput. Method Appl. M., 197(1-4), 232-242 (2007).
https://doi.org/10.1016/j.cma.2007.07.025

B. Teng, R. Eatock Taylor, “New higher order boundary element method for wave diffraction/radiation,” Appl. Ocean Res., 17(2), 71-77 (1995).
https://doi.org/10.1016/0141-1187(95)00007-N

B. Teng, S. Kato, “A method for second-order diffraction potential from an axisymmetric body,” Ocean Eng., 26(12),1369-1387 (1999).
https://doi.org/10.1016/S0029-8018(98)00032-8

B. Teng, S. Kato, “Third order wave force on axisymmetric bodies,” Ocean Eng., 29, 815-843

(2002).
https://doi.org/10.1016/S0029-8018(01)00047-6

L. Wang, R. W. Yeung, “An efficient hybrid integral-equation method for point-absorber wave energy converters with a vertical axis of symmetry,” Appl. Ocean Res., 86, 195-206 (2019).
https://doi.org/10.1016/j.apor.2019.02.010

Y. Wang, Y. Shao, J. Chen, H. Liang, “Accurate and efficient hydrodynamic analysis of structures with sharp edges by the Extended Finite Element Method (XFEM): 2D studies,” Appl. Ocean Res., 117, 102893 (2021).
https://doi.org/10.1016/j.apor.2021.102893

J. P. Wolf, C. Song, “Finite element modelling of unbounded media,” Wiley: Chichester (1996).

G. X. Wu, R. Eatock Taylor, “Finite element analysis of two-dimensional non-linear transient water waves,” Appl. Ocean Res., 16(6), 363-372 (1994).
https://doi.org/10.1016/0141-1187(94)00029-8

C. Yang, R. C. Ertekin, “Numerical simulation of nonlinear wave diffraction by a vertical cylinder,” ASME. J. Offshore Mech. Arct. Eng. February, 114(1), 36–44 (1992).

https://doi.org/10.1115/1.2919950

J. Yang, B. Teng, Y. Gou, “Comparative study on numerical computation methods for radiation forces on a three-dimensional body with edge in the time domain,” ASME. J. Offshore Mech. Arct. Eng., 142(4), 041901 (2020).
https://doi.org/10.1115/1.4045856

Z. J. Yang, A. J. Deek, H. Hao, “A Frobenius solution to the scaled boundary finite element equations in frequency domain for bounded media,” Int. Numer. Meth. Eng., 70(12), 1387-1408 (2007).
https://doi.org/10.1002/nme.1926

Z. J. Yang, E. T. Ooi, “Recent progress in modeling crack propagation using the scaled boundary finite element method,” Int. J. Comput. Methods, 9(1), 1240016 (2012).
https://doi.org/10.1142/S0219876212400166

R. W. Yeung, “Added mass and damping of a vertical cylinder in finite-depth waters,” Appl. Ocean Res., 3(3), 119-133 (1981).
https://doi.org/10.1016/0141-1187(81)90101-2

B. Yu, W. Sun, P. Wei, G. Cao, Z. Hu, J. Zhang, “The scaled boundary finite element method based

921 on the hybrid quadtree mesh for solving transient heat conduction problems," Appl. Math. Model.,
922 89, 541-571 (2021).
923 https://doi.org/10.1016/j.apm.2020.07.035
924
925 R. Zhao, O. M. Faltinsen, "Interaction between current, waves and marine structures," 5th Int. Conf.
926 on Num. Ship Hydrodyn., Hiroshima, National Academy Press, Washington D.C., 1989, 513-525
927 (1989).
928
929 S. Zheng, H. Liang, S. Michele, D. Greaves, "Water wave interaction with an array of submerged
930 circular plates: Hankel transform approach," Phys. Rev. Fluid, 8, 014803 (2023)
931 https://doi.org/10.1103/PhysRevFluids.8.014803